7430 *Inorg. Chem.* **2009**, *48*, 7430–7445
DOI: 10.1021/ic900936p

Inorganic Chemistry
Article

Octahedral Monodithiolene Complexes of Iron: Characterization of *S,S′*-Coordinated Dithiolate(1−) π Radical Monoanions: A Spectroscopic and Density Functional Theoretical Investigation

Carsten Milsmann,[†] Goutam Kumar Patra,[‡] Eckhard Bill,[†] Thomas Weyhermüller,[†] Serena DeBeer George,[§] and Karl Wieghardt*[,†]

[†]*Max-Planck-Institut für Bioanorganische Chemie, Stiftstrasse 34-36, D-45470 Mülheim an der Ruhr, Germany,* [‡]*Department of Chemistry, Vijoygarh Jyotish Ray College, Jadavpur University, Kolkata 700032, India, and* [§]*Stanford Synchrotron Radiation Lightsource, SLAC, Stanford University, Stanford, California 94309*

Received May 13, 2009

The reaction of *cis*-[Fe^{III}(cyclam)Cl_2]Cl with 1 equiv of sodium *N*-diethyldithiocarbamate, toluene-3,4-dithiolate, and maleonitriledithiolate in methanol in the presence of triethylamine afforded the cations [Fe^{III}(cyclam)(Et_2dtc)]$^{2+}$ (**1**), [Fe^{III}(cyclam)(tdt)]$^{+}$ (**2**), and [Fe^{III}(cyclam)(mnt)]$^{+}$ (**3**), which were isolated as triflate, hexafluorophosphate, and tetrafluoroborate salt, respectively, using sodium triflate, potassium hexafluorophosphate, or sodium tetrafluoroborate as the source for the counteranion. Complexes **1**, **2**, and **3** possess an S = $^1/_2$ ground state (low-spin ferric d^5). These salts were characterized by X-ray crystallography, UV−vis, Mössbauer, and electron paramagnetic resonance spectroscopies. Cyclic voltammetry revealed that **2** and **3** are reversibly one-electron-reduced, generating neutral $\mathbf{2^{red}}$ and $\mathbf{3^{red}}$, respectively, and one-electron-oxidized, generating dicationic $\mathbf{2^{ox}}$ and $\mathbf{3^{ox}}$, respectively. Fe and S K-edge X-ray absorption spectroscopy (XAS) revealed that **2** ($S = {}^1/_2$) and $\mathbf{2^{ox}}$ ($S = 0$) possess a low-spin ferric ion. Complexes **2** and **3** are *S,S′*-coordinated to a closed-shell dithiolate(2−) ligand, whereas $\mathbf{2^{ox}}$ and $\mathbf{3^{ox}}$ consist of a low-spin ferric ion antiferromagnetically coupled to a dithiolate(1−) π radical ligand. They are singlet diradicals [Fe^{III}(cyclam)(dithiolate$^{\bullet}$)]$^{2+}$. The analysis of the sulfur K pre-edge transitions reveals significant multiplet effects in the spectra of **2** and $\mathbf{2^{ox}}$, which provide rare experimental evidence for a singlet diradical description for $\mathbf{2^{ox}}$. Mössbauer spectroscopy on frozen solutions of $\mathbf{2^{red}}$ clearly show the presence of a high-spin ferrous ion (S = 2). The experimentally established electronic structures of the three members of the electron transfer series [Fe(cyclam)(dithiolate)]$^{2+,+,0}$ have been verified by broken symmetry density functional theoretical calculations, which have been calibrated against the experiment by calculating XAS and Mössbauer spectra.

Introduction

In a recent report, we showed[1] that it is possible to electrochemically generate the one-electron oxidized forms of [Co^{III}(tren)(bdt)]$^{+}$ ($S = 0$) and [Cr^{III}(tren)(bdt)]$^{+}$ ($S = {}^3/_2$), namely, the corresponding dications. The redox-innocent tetradentate nitrogen donor ligand tren is tris(2-aminoethyl)amine, and $(bdt)^{2-}$ represents benzene-1,2-dithiolate(2−). Both ligands are closed-shell entities at this stage. It was shown by spectroscopy (electron paramagnetic resonance (EPR), UV−vis) and density functional calculations that the monocations are classical Werner-type complexes with a central low-spin cobalt(III) (d^6, $S_{Co} = 0$) and chromium(III) ion (d^3, $S_{Cr} = {}^3/_2$) and closed-shell ligands, neutral tren and a diamagnetic $(bdt)^{2-}$. In contrast, the dications contain a single *S,S′*-coordinated π radical monoanion $(bdt^{\bullet})^{-}$. [Co^{III}(tren)(bdt$^{\bullet}$)]$^{2+}$ ($S = {}^1/_2$) and [Cr^{III}(tren)(bdt$^{\bullet}$)]$^{2+}$ ($S = 1$) have been spectroscopically characterized in solution. It emerged that, in these compounds, the benzene-1,2-dithiolates behave exactly analogous to the corresponding complexes with an *O,O′*-coordinated catecholate(2−) or *o*-benzosemiquinonate(1−) ligand.[2,3]

Here, we report on a similar series of iron(III) complexes, **1**−**3** (Scheme 1), where a redox-innocent, closed-shell cyclam ligand (1,4,8,11-tetraazacyclotetradecane) and a potentially redox-noninnocent dithiolene ligand such as toluene-3,4-dithiolate or maleonitriledithiolate are coordinated to a low-spin ferric ion, affording the octahedral monocations

*To whom correspondence should be addressed. E-mail: wieghardt@mpi-muelheim.mpg.de.

(1) Milsmann, C.; Bothe, E.; Bill, E.; Weyhermüller, T.; Wieghardt, K. *Inorg. Chem.* **2009**, [Online] DOI: 10.1021/ic900515j.

(2) (a) Wicklund, P. A.; Beckmann, L. S.; Brown, D. G. *Inorg. Chem.* **1976**, *15*, 1996. (b) Wicklund, P. A.; Brown, D. G. *Inorg. Chem.* **1976**, *15*, 396.

(3) (a) Wheeler, D. E.; McCusker, J. K. *Inorg. Chem.* **1998**, *37*, 2296. (b) Rodriguez, J. H.; Wheeler, D. E.; McCusker, J. K. *J. Am. Chem. Soc.* **1998**, *120*, 12051.

Published on Web 07/02/2009

Scheme 1. Ligands and Complexes

Complexes

$[Fe^{III}(cyclam)(Et_2dtc)](BPh_4)_2 \cdot H_2O$	($S = {}^1/_2$)	$\mathbf{1}(BPh_4)_2 \cdot H_2O$
$[Fe^{III}(cyclam)(Et_2dtc)](OTf)_2 \cdot CH_3CN$	($S = {}^1/_2$)	$\mathbf{1}(OTf)_2 \cdot CH_3CN$
$[Fe^{III}(cyclam)(tdt)](PF_6)$	($S = {}^1/_2$)	$\mathbf{2}(PF_6)$
$[Fe^{III}(cyclam)(mnt)](BF_4)$	($S = {}^1/_2$)	$\mathbf{3}(BF_4)$

Ligands

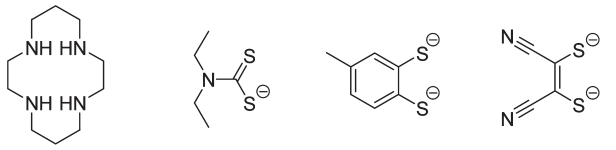

(cyclam) $(Et_2dtc)^{1-}$ $(tdt)^{2-}$ $(mnt)^{2-}$

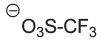

$(OTf)^{1-}$

2 and **3**. In order to study the electronic structure of such species containing only redox-stable ligands, we also synthesized the dication $[Fe^{III}(cyclam)(Et_2dtc)]^{2+}$ (**1**), where $(Et_2dtc)^-$ is the closed-shell, diamagnetic anion *N*-diethyldithiocarbamate(1−). Only a few such complexes containing a *cis*-$[Fe^{III}N_4S_2]$ core structure have been reported previously: $[Fe^{III}(L\text{-}N_4Me_2)(bdt)]^+$ ($L\text{-}N_4Me_2$ = *N,N′*-dimethyl-2,11-diaza[3.3]-(2,6)pyridinophane),[4] $[Fe^{III}(tripod)(bdt)]^+$ (tripod = tris[(2-pyridyl)methyl] amine, and bis[(2-pyridyl)methyl][(1-methylimidazole-2-yl)-methyl]amine[5] $[(bdt)^{2-}$ is unsubstituted benzene-1,2-dithiolate (2−)]. The former low-spin ferric compound exhibits an unusual thermal spin transition from an $S = {}^1/_2$ low-spin ground state to an $S = {}^3/_2$ intermediate-spin excited state.[4] No data on either the oxidized or reduced form of this complex have been published to date. The same is true for the series of monodithiolene iron complexes employing tripodal N_4 ligands reported recently by Rompel et al.[5]

The monocationic complexes **2** and **3** of the present series possess an $S = {}^1/_2$ ground state (low-spin ferric), and their electrochemistry reveals that a stable one-electron oxidized dication $[Fe(cyclam)(dithiolene)]^{2+}$ and a stable one-electron reduced neutral species exist in solution. The electronic structures of each of the members of these electron transfer series $[Fe(cyclam)(dithiolene)]^z$ ($z = 2+, +, 0$) have been experimentally established by X-ray crystallography, Mössbauer, EPR, and UV−vis spectroscopies, as well as by X-ray absorption spectroscopy (XAS) (Fe K-edge, S K-edge). Finally, we have corroborated the experimental results by broken symmetry (BS) density functional theoretical (DFT) calculations using the B3LYP functional.

Experimental Section

Preparation of Complexes. The starting material *cis*-$[Fe^{III}(cyclam)Cl_2]Cl$ and its ^{57}Fe-enriched analogue have been prepared as described in the literature.[6,7] The ligands were commercially available.

$[Fe^{III}(cyclam)(Et_2dtc)](BPh_4)_2 \cdot H_2O$ ($1(BPh_4)_2 \cdot H_2O$). Under an argon blanketing atmosphere, a solution of $Na(Et_2dtc)$ (63 mg, 0.28 mmol) in degassed methanol (10 mL) was slowly added to a solution of *cis*-$[Fe(cyclam)Cl_2]Cl$ (100 mg, 0.28 mmol) in a degassed methanol/water mixture (2:1, 30 mL). After stirring for 2 h, a solution of $NaBPh_4$ (205 mg, 0.6 mmol) dissolved in degassed methanol (3 mL) was added. A microcrystalline, red solid precipitated immediately, which was filtered off, washed with methanol/water (3:1) and diethyl ether, and air-dried. The product is air-stable in the solid state. Yield: 182 mg (62%); Anal. Calcd for $C_{63}H_{76}B_2FeN_5OS_2$: C, 71.32; H, 7.22; N, 6.60. Found: C, 71.44; H, 7.24; N, 6.60.

$[Fe^{III}(cyclam)(Et_2dtc)](OTf)_2 \cdot MeCN$ ($1(OTf)_2$ MeCN). This salt was prepared according to the procedure described for $\mathbf{1}(BPh_4)_2 \cdot H_2O$ by using sodium triflate (NaOTf) instead of $NaBPh_4$. Single crystals were obtained from slow evaporation of a concentrated solution of $\mathbf{1}(OTf)_2$ in MeCN. Anal. Calcd for $C_{19}H_{37}F_6FeN_6O_6S_4$: C, 30.69; H, 5.02; N, 11.30; Fe, 7.51. Found: C, 30.57; H, 5.08; N, 11.42; Fe, 7.48.

$[Fe^{III}(cyclam)(tdt)](PF_6)$ ($2(PF_6)$). To a solution of *cis*-$[Fe(cyclam)Cl_2]Cl$ (363 mg, 1 mmol) in a methanol/water mixture (2:1, 90 mL) was added dropwise a degassed methanolic solution (10 mL) of H_2tdt and NEt_3 (420 μL, 3 mmol) with constant stirring under an Ar blanketing atmosphere. The purple mixture was stirred at room temperature for 1 h, after which it was filtered. An aqueous solution of KPF_6 (275 mg, 1.5 mmol) was added, and stirring was continued for 2 h. Upon slow evaporation of the solvent under a flow of Ar, purple crystals were obtained. Yield: 383 mg (69%). Anal. Calcd for $C_{17}H_{30}F_6FeN_4PS_2$: C, 36.76; H, 5.44; N, 10.09; Fe, 10.06. Found: C, 36.59; H, 5.30; N, 10.24; Fe, 10.12.

$[Fe^{III}(cyclam)(mnt)](BF_4)$ ($3(BF_4)$). *cis*-$[Fe(cyclam)Cl_2]Cl$ (363 mg, 1 mmol) was dissolved in methanol/water (2:1, 90 mL), and argon was purged through the solution for 15 min. Na_2mnt (185 mg, 1 mmol) was dissolved in degassed methanol (10 mL), and triethylamine (420 μL, 3 mmol) was added to the Na_2mnt solution. The Na_2mnt−triethylamine mixture was added dropwise with constant stirring to the *cis*-$[Fe(cyclam)Cl_2]Cl$ solution, and stirring was continued for 2 h at room temperature. The solution was filtered, and potassium hexafluorophosphate (275 mg, 1.5 mmol) was added to the filtrate. After 1 h, the greenish-brown precipitate was filtered, washed with water, and stored under argon. Single crystals suitable for an X-ray crystallographic analysis were selected from the crystalline product. Yield: 422 mg (78%). Anal. Calcd for $C_{14}H_{24}F_6FeN_6PS_2$: C, 31.04; H, 4.47; N, 15.52; S, 11.85; Fe, 10.32. Found: C, 31.02; H, 4.40; N, 15.57; S, 11.92; Fe, 10.18%.

X-Ray Crystallographic Data Collection and Refinement of the Structures. A dark red single crystal of $\mathbf{1}(OTf)_2 \cdot MeCN$, a dark blue-violet crystal of $\mathbf{2}(PF_6)$, and a dark green specimen of $\mathbf{3}(BF_4)$ were coated with perfluoropolyether, picked up with nylon loops, and mounted in the nitrogen cold stream of a Bruker-Nonius KappaCCD diffractometer equipped with a Mo-target rotating-anode X-ray source. Graphite monochromated Mo Kα radiation ($\lambda = 0.71073$ Å) was used throughout. Final cell constants were obtained from least-squares fits of several thousand strong reflections. Intensities of redundant reflection were used to correct for absorption using the program SADABS.[8] The structures were readily solved by Patterson methods and subsequent difference Fourier techniques. The Siemens ShelXTL software package[9] was used for solution

(4) Koch, W. O.; Schünemann, V.; Gerdan, M.; Trautwein, A. X.; Krüger, H.-J. *Chem. Eur. J.* **1998**, *4*, 686.
(5) Merkel, M.; Pascaly, M.; Wieting, M.; Duda, M.; Rompel, A. *Z. Anorg. Allg. Chem.* **2003**, *629*, 2216.
(6) Chan, P.-K.; Poon, C.-K. *J. Chem. Soc., Dalton Trans.* **1976**, 858.
(7) Meyer, K.; Bill, E.; Mienert, B.; Weyhermüller, T.; Wieghardt, K. *J. Am. Chem. Soc.* **1999**, *121*, 4859–4876.
(8) *SADABS*, version 2006/1; Bruker AXS Inc.: Madison, WI, 2007.
(9) *ShelXTL*, version 6.14; Bruker AXS Inc.: Madison, WI, 2003.

Table 1. Crystallographic Data for **1**·MeCN, **2**, and **3**

	1$(OTf)_2$·MeCN	**2**(PF_6)	**3**$(BF)_4$
chem. formula	$C_{19}H_{37}F_6FeN_6O_6S_4$	$C_{17}H_{30}F_6FeN_4PS_2$	$C_{14}H_{24}BF_4FeN_6S_2$
cryst size, mm^3	$0.18 \times 0.08 \times 0.06$	$0.09 \times 0.03 \times 0.03$	$0.07 \times 0.02 \times 0.02$
fw	743.64	555.39	483.17
space group	$P\bar{1}$, No. 2	$P\bar{1}$, No. 2	$P2_1/n$, No.14
a, Å	9.1969(3)	8.7110(3)	8.5350(3)
b, Å	11.6996(4)	9.6927(4)	12.2605(4)
c, Å	14.5177(4)	13.7946(7)	18.9435(6)
α, deg	89.832(2)	79.162(4)	90
β, deg	82.675(2)	75.570(4)	98.786(3)
γ, deg	83.205(2)	87.115(4)	90
V, Å	1538.36(8)	1107.85(8)	1959.05(11)
Z	2	2	4
T, K	100(2)	100(2)	100(2)
ρ calcd, g cm^{-3}	1.605	1.665	1.638
reflns collected/$2\Theta_{max}$	37258/65.00	15958/65.00	37258/66.32
unique reflns/$I > 2\sigma(I)$	11108/9160	8000/6917	7433/6176
no. of params/restraints	382/0	324/34	253/0
λ, Å /μ(Kα), cm^{-1}	0.71073/8.43	0.71073/10.05	0.71073/10.33
R1[a]/goodness of fit[b]	0.0330/1.031	0.0523/1.106	0.0320/1.019
wR2[c] ($I > 2\sigma(I)$)	0.0775	0.1078	0.0687
residual density, e$Å^{-3}$	+0.56/−0.42	+0.76/−1.15	+0.48/- 0.47

[a] Observation criterion: $I > 2\sigma(I)$, $R1 = \sum ||F_o| - |F_c|| / \sum |F_o|$. [b] $GoF = [\sum w(F_o^2 - F_c^2)^2]/(n-p)]^{1/2}$. [c] $wR2 = [\sum w(F_o^2 - F_c^2)^2]/\sum[w(F_o^2)^2]]^{1/2}$, where $w = 1/\sigma^2(F_o^2) + (aP)^2 + bP$, $P = (F_o^2 + 2F_c^2)/3$.

and artwork of the structures; ShelXL97[10] was used for the refinement. All non-hydrogen atoms were anisotropically refined, and hydrogen atoms were placed at calculated positions and refined as riding atoms with isotropic displacement parameters.

The cyclam ligand in **2** was found to be disordered over two sites by a 90° rotation. The occupation ratio refined to about 0.50:0.50. Corresponding disordered carbon and nitrogen atoms of the split model were refined with equal thermal displacement parameters and restrained bond lengths using the SAME instruction of ShelXL97 (34 restraints). Crystallographic data of the compounds are listed in Table 1.

Physical Measurements. Elemental analyses were measured at the Mikroanalytisches Labor H. Kolbe, in Mülheim an der Ruhr, Germany. Cyclic voltammograms and square wave voltammograms in the range of −25 to +25 °C were recorded by using an EG&G Potentiostat/Galvanostat 273A. A three-electrode cell was employed with a glassy-carbon working electrode, a glassy-carbon auxiliary electrode, and a $Ag/AgNO_3$ reference electrode (0.01 M $AgNO_3$ in CH_3CN). Ferrocene was added as an internal standard after completion of the measurements, and potentials are referenced versus the Fc^+/Fc couple. Controlled potential coulometric measurements were performed in a setup, which allows recording of absorption spectra in situ during electrolysis, by employing the same potentiostat, but using a Pt grid as a working electrode. A Pt brush was used as a counterelectrode and separated from the working electrode compartment by a Vycor frit. A $Ag/AgNO_3$ (0.01 M $AgNO_3$ in CH_3CN) reference electrode was employed again. UV−vis spectra were measured on a Hewlett-Packard 8452A diode array spectrophotometer. Temperature-dependent magnetic susceptibilities were measured by using a SQUID magnetometer (MPMS Quantum Design) at 1.0 T (4−300 K). Underlying diamagnetism was corrected by using tabulated Pascal's constants. X-band EPR derivative spectra were recorded on a Bruker ELEXSYS E500 spectrometer equipped with the Bruker standard cavity (ER4102ST) and a helium flow cryostat (Oxford Instruments ESR 910). Microwave frequencies were calibrated with a Hewlett-Packard frequency counter (HP5352B), and the field control was calibrated with a Bruker NMR field probe (ER035M). The spectra were simulated with the program GFIT (by Eckhard Bill) for the calculation of powder spectra with effective g values and anisotropic line widths (Gaussian line shapes were used). Mössbauer data were recorded on a spectrometer with alternating constant acceleration. The minimum experimental line width was 0.24 mm s^{-1} (full width at half-height). The sample temperature was maintained constant either in an Oxford Instruments Variox or an Oxford Instruments Mössbauer-Spectromag cryostat. The latter is a split-pair superconducting magnet system for applied fields up to 8 T, where the temperature of the sample can be varied in the range 1.5−250 K. The field at the sample is perpendicular to the γ beam. Isomer shifts are quoted relative to iron metal at 300 K. Magnetic Mössbauer spectra were simulated with the progam MX (by Eckhard Bill).

X-Ray Absorption Spectroscopy Measurements and Data Analysis. All data were measured at the Stanford Synchrotron Radiation Laboratory under the ring conditions of 3.0 GeV and 60−100 mA. All S K-edge data were measured using the 54-pole wiggler beamline 6−2 in the high magnetic field mode of 10 kG with a Ni-coated harmonic rejection mirror and a fully tuned Si-(111) double-crystal monochromator. Details of the optimization of this setup have been previously described.[11] Data were measured at room temperature by fluorescence, using a Lytle detector. To check for reproducibility, two to three scans were measured for each sample. The energy was calibrated from S K-edge spectra of $Na_2S_2O_3 \cdot 5H_2O$, run at intervals between sample scans. The maximum of the first pre-edge feature in the spectrum was fixed at 2472.02 eV. A step size of 0.08 eV was used over the edge region. Data were averaged, and a smooth background was removed from all spectra by fitting a polynomial to the pre-edge region and subtracting this polynomial from the entire spectrum. Normalization of the data was accomplished by fitting a flattened polynomial or straight line to the postedge region (2490−2740 eV) and normalizing the postedge at 1.0.

Fe K-edge XAS data were measured on focused 16-pole wiggler beamline 9−3. A Si(220) monochromator was utilized for energy selection. A Rh-coated harmonic rejection mirror set to a 10 keV cutoff was used to minimize higher harmonics. All samples were prepared as solids in boron nitride, pressed into

(10) Sheldrick, G. M. *ShelXL97*; University of Göttingen: Göttingen, Germany, 1997.

(11) Hedman, B.; Frank, P.; Gheller, S. F.; Roe, A. L.; Newton, W. E.; Hodgson, K. O. *J. Am. Chem. Soc.* **1998**, *110*, 3798.

a pellet, and sealed between 38 μm Kapton tape windows in a 1 mm aluminum spacer. The samples were maintained at 10 K during data collection using an Oxford Instruments CF1208 continuous-flow liquid helium cryostat. Data were measured in transmission mode. Internal energy calibrations were performed by simultaneous measurement of an Fe reference foil placed between a second and third ionization chamber. The first inflection point was assigned to 7111.2 eV for Fe. Data represent three to five scan averages and were processed by fitting a second-order polynomial to the pre-edge region and subtracting this background from the entire spectrum. A three-region cubic spline was used to model the smooth background above the edge. The data were normalized by subtracting the spline and normalizing the postedge to 1.0. The spectra were deconvoluted using the program EDG_FIT.[12]

Calculations. All DFT calculations were performed with the ORCA[13] program package. The geometry optimizations of the complexes and single-point calculations on the optimized geometries were carried out using the B3LYP[14] functional. This hybrid functional often gives better results for transition metal compounds than pure gradient-corrected functionals, especially with regard to metal−ligand covalency.[15] The all-electron Gaussian basis sets were those developed by the Ahlrichs group.[16,17] Triple-ζ-quality basis sets, TZV(P), with one set of polarization functions on the metals and on the atoms directly coordinated to the metal center were used.[16] For the carbon and hydrogen atoms, slightly smaller polarized split-valence, SV(P), basis sets were used, which were of double-ζ quality in the valence region and contained a polarizing set of d functions on the non-hydrogen atoms.[17] Auxiliary basis sets used to expand the electron density in the resolution-of-the-identity approach were chosen,[18] where applicable, to match the orbital basis. The self-consistent field calculations were tightly converged (1×10^{-8} E_h in energy, 1×10^{-7} E_h in the density change, and 1×10^{-7} in maximum element of the DIIS error vector). The geometry optimizations for all complexes were carried out in redundant internal coordinates without imposing symmetry constraints. In all cases, the geometries were considered converged after the energy change was less than 5×10^{-6} E_h. The gradient norm and maximum gradient element were smaller than 1×10^{-4} E_h Bohr^{-1} and 3×10^{-4} E_h Bohr^{-1}, respectively, and the root-mean square and maximum displacements of all atoms were smaller than 2×10^{-3} Bohr and 4×10^{-3} Bohr, respectively. Throughout this paper, we describe our computational results by using the BS approach of Ginsberg[19] and Noodleman et al.[20] Since several broken symmetry solutions to the spin-unrestricted Kohn−Sham equations may be obtained, the general notation BS(m,n)[21] has been adopted, where (m,n) denotes the number of spin-up and spin-down electrons at the two interacting fragments. Canonical and corresponding orbitals,[22] as well as spin density plots, were generated with the program Molekel.[23] Nonrelativistic single-point calculations on the optimized geometry were carried out to predict Mössbauer spectral parameters (isomer shifts and quadrupole splittings). These calculations employed the CP(PPP) basis set[24] for iron. The Mössbauer isomer shifts were calculated from the computed electron densities at the iron centers, as previously described.[25] Time-dependent DFT (TD-DFT) calculations were performed to predict the transitions in the pre-edge region of the S and Fe K-edge XAS spectra.[26] The symmetry equivalent 1s orbitals obtained from the ground state calculations were localized using the Pipek−Mezey criteria,[27] and TD-DFT calculations at the B3LYP or BP86 level were performed, allowing only for excitations from the localized sulfur 1s orbitals. The basis sets were chosen to match the basis sets used for the single-point ground state calculations. The obtained S K-edge transition energies were corrected by a constant 56.3 eV (B3LYP) or 76.0 eV (BP86) shift to align calculated spectra with experimental spectra. For the Fe K-edge calculations, a constant shift of 150.2 eV (B3LYP) was applied.

Results and Discussion

a. Synthesis and Characterization of Complexes. Upon slow addition of 1 equiv of $NaEt_2dtc$ to *cis*-[Fe^{III}(cyclam)Cl_2]Cl in a methanol/water mixture (2:1) in the absence of oxygen, a red solution was obtained. Sodium triflate (NaOTf) was added and the solvents were removed in vacuo. The remaining solid residue was redissolved in acetonitrile. After filtration, the red crystalline product [Fe(cyclam)(Et_2dtc)](OTf)$_2\cdot$MeCN, **1**(OTf)$_2\cdot$MeCN, was obtained by slow evaporation of the solvent. Alternatively, the tetraphenylborate salt of **1** was obtained directly from the reaction mixture after addition of $NaBPh_4$ (yield 62%). The salt **1**(BPh_4)$_2\cdot H_2O$ was used exclusively for the XAS experiments. The remaining physical measurements for **1** were conducted using **1**(OTf)$_2\cdot$MeCN. For ligand abbreviations, see Scheme 1.

The compound [Fe(cyclam)(tdt)]$^+$, **2**, was obtained by slow addition of 1 equiv of H_2tdt dissolved in methanol to a solution of *cis*-[Fe^{III}(cyclam)Cl_2]Cl in methanol/water in the presence of 2 equiv of KO^{t}Bu. The initial yellow color of the reaction mixture quickly developed a new color, which eventually led to a dark purple solution. The addition of KPF_6 and slow evaporation of the solvent afforded dark red crystals of **2**(PF_6), suitable for X-ray crystallography (yield 69%). The compound is air-stable in the solid state but decomposes slowly in solution. For Mössbauer experiments, an ^{57}Fe labeled sample was prepared following the same experimental procedure but using [^{57}Fe(cyclam)Cl_2]Cl as the starting material.

Similarly, [Fe(cyclam)(mnt)]$^+$, **3**, was obtained by using Na_2mnt under the same conditions as described for **2**. It was isolated as a green crystalline solid, **3**(BF_4), after the addition of $NaBF_4$.

(12) George, G. N. *EXAFSPAK & EDG_FIT*; Stanford Synchrotron Radiation Laboratory, Stanford Linear Accelerator Center, Stanford University: Stanford, CA, 2000.
(13) Neese, F. *Orca-an ab initio, DFT and Semiempirical Electronic Structure Package*, version 2.6, revision 4; Institut für Physikalische und Theoretische Chemie, Universität Bonn: Bonn, Germany, 2007.
(14) (a) Becke, A. D. *J. Chem. Phys.* **1993**, *98*, 5648–52. (b) Becke, A. D. *J. Chem. Phys.* **1986**, *84*, 4524. (c) Lee, C. T.; Yang, W. T.; Parr, R. G. *Phys. Rev. B* **1988**, *37*, 785.
(15) Neese, F.; Solomon, E. I. In *Magnetism: From Molecules to Materials*; Miller, J. S., Drillon, M., Eds.; Wiley: New York, 2002; Vol. *4*, p 345.
(16) Schäfer, A.; Huber, C.; Ahlrichs, R. *J. Chem. Phys.* **1994**, *100*, 5829.
(17) Schäfer, A.; Horn, H.; Ahlrichs, R. *J. Chem. Phys.* **1992**, *97*, 2571.
(18) (a) Eichkorn, K.; Weigend, F.; Treutler, O.; Ahlrichs, R. *Theor. Chem. Acc.* **1997**, *97*, 119–124. (b) Eichkorn, K.; Treutler, O.; Öhm, H.; Häser, M.; Ahlrichs, R. *Chem. Phys. Lett.* **1995**, *240*, 283. (c) Eichkorn, K.; Treutler, O.; Öhm, H.; Häser, M.; Ahlrichs, R. *Chem. Phys. Lett.* **1995**, *242*, 652.
(19) Ginsberg, A. P. *J. Am. Chem. Soc.* **1980**, *102*, 111.
(20) Noodleman, L.; Peng, C. Y.; Case, D. A.; Mouesca, J. M. *Coord. Chem. Rev.* **1995**, *144*, 199.
(21) Kirchner, B.; Wennmohs, F.; Ye, S.; Neese, F. *Curr. Opin. Chem. Biol.* **2007**, *11*, 134.
(22) Neese, F. *J. Phys. Chem. Solids* **2004**, *65*, 781–785.
(23) Molekel. Advanced Interactive 3D-Graphics for Molecular Sciences, available at http:\\www.cscs.ch/molekel/ (accessed June 2009).
(24) Neese, F. *Inorg. Chim. Acta* **2002**, *337*, 181–192.
(25) Sinnecker, S.; Slep, L. D.; Bill, E.; Neese, F. *Inorg. Chem.* **2005**, *44*, 2245–2254.
(26) DeBeer George, S.; Petrenko, T.; Neese, F. *Inorg. Chim. Acta* **2008**, *361*, 965.
(27) Pipek, J.; Mezey, P. G. *J. Chem. Phys.* **1989**, *90*, 4916.

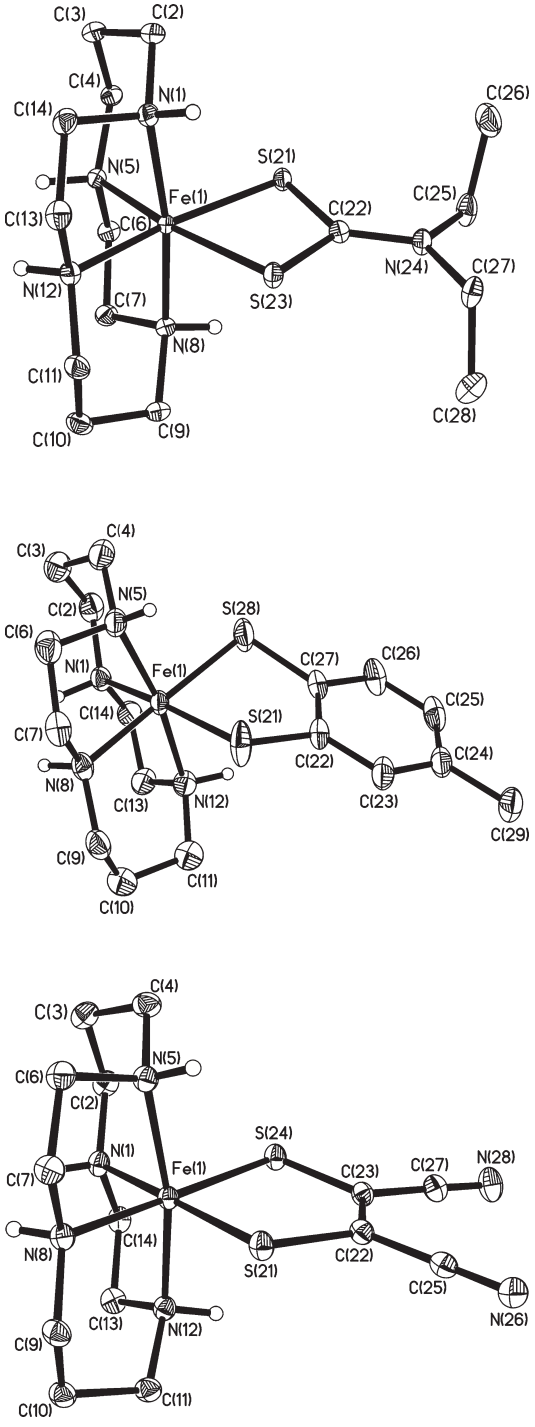

Figure 1. Structure and numbering scheme of the dication **1** in **1**$(OTF)_2\cdot CH_3CN$ and the monocations **2** and **3** in **2**(PF_6) and **3**(BF_4). Thermal ellipsoids are drawn at the 50% probability level. The C−H hydrogen atoms are omitted for clarity.

b. Crystal Structures. The structures of the complexes **1**$(OTf)_2\cdot$MeCN, **2**(PF_6), and **3**(BF_4) have been determined by X-ray crystallography at 100(2) K. The crystallographic details are provided in Table 1. The structures of the cations **1**, **2**, and **3** are shown in Figure 1, and selected bond distances are given in Table 2. In all complexes, the central iron ion has a distorted octahedral *cis*-FeN_4S_2-coordination sphere. The cyclam ligand is coordinated in the *cis* configuration, leaving two adjacent sites free for the bidentate sulfur ligand. The Fe−N bond distances are in the range of 1.985(5)−2.102(3) Å, which is compatible with the presence of a low-spin ferric metal ion.[7,28−30] It is noteworthy that in the corresponding high-spin ions the Fe−N bond distances are observed in the range of 2.15−2.21 Å.[7,28,30]

As is to be expected for a redox-innocent, closed-shell dithiocarbamate(1−) ligand, the structural parameters (C−S and C(22)−N(24) bond lengths) of the *S*,*S*′-coordinated ligand in **1** are in excellent agreement with the values reported for the uncoordinated Et_2dtc^- ligand.[31] The two equidistant C−S bonds indicate complete delocalization in the S_2CN π system, which is also reflected in the short C(22)−N(24) distance, exhibiting partial double-bond character. Therefore, all structural parameters indicate that the ligand is coordinated in its closed-shell monoanionic form. Since **1** is a dication, the iron center must contain a ferric ion with a d^5 electron configuration.

The inspection of the crystal packing of **1**$(OTf)_2\cdot$MeCN reveals that the cations are well-separated by triflate counteranions and exhibit no direct interactions.

The average C−S bond length in **2** (1.752(2) Å) is significantly longer than expected for an *o*-dithiobenzosemiquinonate(1−) radical (1.72−1.73 Å)[32] but is shorter than that observed for the closed-shell dithiolene ligands in $[Co^{III}(tren)(bdt)]^+$ and $[Cr^{III}(tren)(bdt)]^+$.[1] This is most probably due to an unresolved disorder of the dithiolate(2−) ligand (unrealistically large anisotropic thermal parameters of the sulfur atoms are observed). In agreement with the spectroscopic results (see below), the ligand is described as a closed-shell dianion. Thus, the metal ion has also a +III oxidation state, and therefore, complex **2** is best described as a low-spin d^5 ferric compound. This is also in agreement with the large value for the fold angle φ (33°), which is a marker for the absence of π interactions between the metal and ligand, as has previously been discussed.[1] The fold angle φ is the dihedral angle between the two planes FeS_2 and S_2C_2; it describes a folding of the planes along the S···S vector.

The C−S bond distances in **3** are short at ∼1.73 Å. However, this is not indicative of the presence of a radical ligand. Due to the strong electron-withdrawing effect of the cyano substituents, the C−S bonds in closed-shell mnt^{2-} ligands are substantially shortened. In fact, the C−S distances in tetrahedral $[Zn^{II}(mnt)_2]^{2-}$ are 1.73−1.74 Å,[33] in agreement with a closed-shell ligand description for **3**. Consequently, **3** is described as a low-spin ferric complex with a closed-shell mnt^{2-} ligand. Nevertheless, the significantly smaller ligand fold angle φ (9.53°) implies stronger π-bonding between the ligand and the central Fe atom in **3** as compared to **2**, resulting in increased delocalization. In fact, the small deviation from planarity might well be a result of crystal packing effects.

(28) Guilard, R.; Siri, O.; Tabard, A.; Broeker, G.; Richard, P.; Nurco, D. J.; Smith, K. M. *J. Chem. Soc., Dalton Trans.* **1997**, 3459–3463.
(29) Ballester, L.; Gutierrez, A.; Perpinan, M. F.; Rico, S.; Azcondo, M. T.; Bellitto, C. *Inorg. Chem.* **1999**, *38*, 4430–4434.
(30) Chun, H.; Bill, E.; Bothe, E.; Weyhermüller, T.; Wieghardt, K. *Inorg. Chem.* **2002**, *41*, 5091.
(31) Mereiter, K.; Preisinger, A. *Inorg. Chim. Acta* **1985**, *98*, 71.
(32) (a) Ray, K.; Weyhermüller, T.; Goossens, A.; Menno, W. J. C.; Wieghardt, K. *Inorg. Chem.* **2003**, *42*, 4082–4087. (b) Ray, K.; Weyhermüller, T.; Neese, F.; Wieghardt, K. *Inorg. Chem.* **2005**, *44*, 5345–5360.
(33) (a) Lewis, G. R.; Dance, I. *J. Chem. Soc., Dalton Trans.* **2000**, 3176–3185. (b) Stach, J.; Kirmse, R.; Sieler, J.; Abram, U.; Dietzsch, W.; Bottcher, R.; Hansen, L. K.; Vergoossen, H.; Gribnau, M. C. M.; Keijzers, C. P. *Inorg. Chem.* **1986**, *25*, 1369.

Table 2. Selected Bond Distances (Å) and Folding Angles φ (deg) in **1**, **2**, and **3**

1		**2**		**3**	
Fe(1)−N(1)	2.0302(11)	Fe(1)−N(5)	1.985(5)	Fe(1)−N(5)	2.0335(11)
Fe(1)−N(5)	2.0509(11)	Fe(1)−N(1)	2.102(3)	Fe(1)−N(1)	2.0855(10)
Fe(1)−N(12)	2.0480(10)	Fe(1)−N(8)	2.064(7)	Fe(1)−N(8)	2.0646(11)
Fe(1)−N(8)	2.0339(11)	Fe(1)−N(12)	2.088(5)	Fe(1)−N(12)	2.0463(11)
Fe(1)−S(21)	2.2902(3)	Fe(1)−S(21)	2.2361(6)	Fe(1)−S(24)	2.2337(4)
Fe(1)−S(23)	2.2909(3)	Fe(1)−S(28)	2.2411(7)	Fe(1)−S(21)	2.2447(3)
S(21)−C(22)	1.7274(13)	S(21)−C(22)	1.754(2)	S(24)−C(23)	1.7278(12)
S(23)−C(22)	1.7296(12)	S(28)−C(27)	1.750(2)	S(21)−C(22)	1.7296(13)
C(22)−N(24)	1.3171(15)	C(22)−C(23)	1.403(3)	C(23)−C(22)	1.3666(17)
		C(23)−C(24)	1.387(3)		
		C(24)−C(25)	1.378(4)		
		C(25)−C(26)	1.384(4)		
		C(26)−C(27)	1.401(3)		
		C(27)−C(22)	1.391(3)		
		φ	33.03	φ	9.53

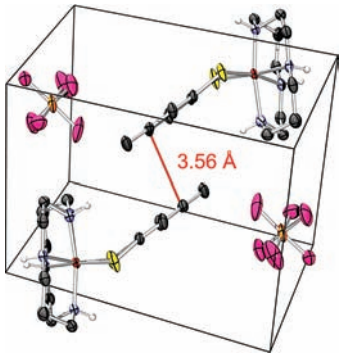

Figure 2. Unit cell of **2**(PF_6) showing the pairwise arrangement of the molecules held together by $\pi-\pi$-stacking interactions. The red line indicates the distances between the two phenyl rings of the interacting cations. C−H hydrogen atoms are omitted for clarity.

Another important feature in the crystal structures of **2**(PF_6) and **3**(BF_4) is the packing motif of both complexes in the solid state. In both structures, a pairwise alignment of two cations is observed. For **2**, this dimer is stabilized by $\pi-\pi$ stacking interactions between the two phenyl rings of the dithiolene ligands (side view, Figure 2; top view, Figure S1, Supporting Information). The distance between the π systems is 3.56 Å, which is typical for $\pi-\pi$ stacks in metal compounds.[34] The Fe−Fe distance in the dimer is 11.64 Å. In contrast, the dimers in **3** are stabilized by two intermolecular hydrogen bonds between a terminal nitrogen atom of the mnt^{2-} ligand of one cation and an amine hydrogen of the cyclam ligand of the other cation, as shown in Figure 3. The Fe−Fe distance in **3** at 8.22 Å is shorter than that in **2**. The side view of the dimer in **3** reveals another important detail. In contrast to **2**, the dithiolene ligands are folding away from the other half of the dimer. This suggests that the small deviation from planarity (φ = 9.53°) in **2** is really a result of crystal packing effects rather than electronic effects.

c. Magnetochemistry and EPR Spectroscopy. The electronic ground states of complexes **1**−**3** have been established from variable-temperature (4−300 K) magnetic susceptibility measurements on powders using a SQUID magnetometer with an applied field of 1.0 T.

The temperature dependence of the effective magnetic moment, μ_{eff}, of **1**$(OTf)_2\cdot$MeCN is shown in Figure 4 (top). Complex **1** shows a nearly temperature-independent μ_{eff} of

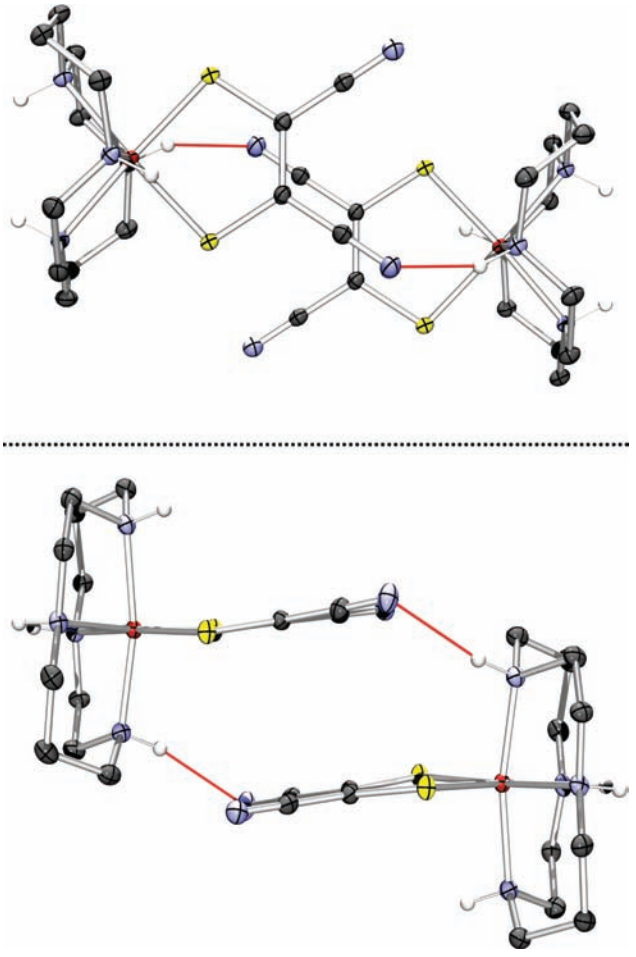

Figure 3. Representation of an interacting pair of monocations in the crystal packing of **3** viewed from the top (top) and from the side (bottom). The stabilizing hydrogen bonds are depicted in red. C−H hydrogen atoms are omitted for clarity.

2.18 μ_B, which is indicative of an $S = {}^1/_2$ ground state. The data in the high-temperature region were readily fit by using a g_{av} of 2.35, a χ_{TIP} of 500×10^{-6} emu, and a small amount of a paramagnetic impurity ($S = {}^5/_2$, 3%). We assume that this impurity is colloidal rust, which may be formed in this type of iron chemistry.[35] Small amounts (< 5%) of such material are generally not observed in

(34) Janiak, C. *J. Chem. Soc., Dalton Trans.* **2000**, 3885.

(35) Roy, N.; Sproules, S.; Bill, E.; Weyhermüller, T.; Wieghardt, K. *Inorg. Chem.* **2008**, *47*, 10911.

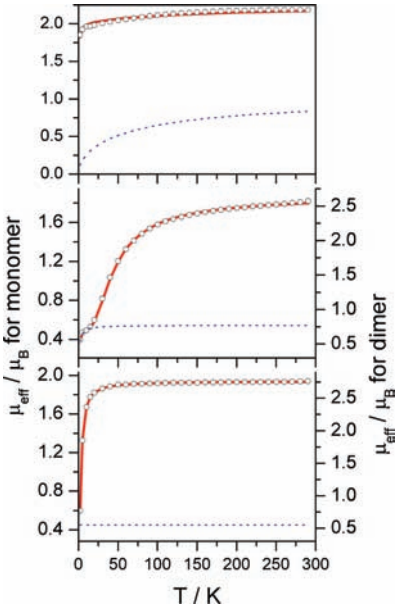

Figure 4. Temperature dependence of the magnetic moment, μ_{eff}, of **1**$(OTf)_2 \cdot$MeCN (top), **2**$(PF)_6$ (middle), and **3**$(BF)_4$ (bottom). The red line represents the spin-Hamiltonian simulation, and the dotted blue line shows the paramagnetic $S = {}^5/_2$ impurity. Fitting parameters are described in the text.

Mössbauer spectroscopy (vide infra), because of intrinsic line broadening due to superparamagnetic relaxation. The remarkably large average g value, g_{av}, is in agreement with the EPR measurements discussed below. For the low-temperature region, very weak intermolecular, antiferromagnetic coupling was taken into account by a small Weiss constant θ of -0.36 K. This is consistent with the structural data (vide supra), which show that the cations are completely separated by the counteranions. Consequently, no superexchange pathway for strong antiferromagnetic coupling via direct contacts is available.

This is in contrast to the situation in **2**. The temperature dependence of the effective magnetic moment, μ_{eff}, of **2**(PF_6) is shown in Figure 4 (middle). While the effective magnetic moment of 1.82 μ_B per Fe ion at 298 K is in good agreement with the spin-only value for an $S = 1/2$ ground state (1.73 μ_B), the strong temperature dependence below 150 K cannot be fitted using a monomer model. Even the implementation of a large Weiss constant fails to reproduce the data in this region. Taking into account the results from the structural analysis, an excellent fit of the data was obtained, by assuming a dimer model where two molecules with a spin ground state of $S = 1/2$ couple intermolecularly. The values for the best fit yielded a g_{av} value of 2.102 for both iron centers, a χ_{TIP} of 224×10^{-6} emu, and an intermolecular antiferromagnetic coupling constant J of -37 cm^{-1}. The fit again required a small paramagnetic impurity (1.7%, $S = {}^5/_2$), for which weak antiferromagnetic coupling was taken into account by a Weiss constant θ_{PI} of -2 K. The coupling constant J is remarkably large, considering that the coupling is mediated only via $\pi-\pi$ stacking interactions of closed-shell ligands.[36] A direct superexchange pathway between the paramagnetic metal centers can be ruled out because of the large Fe−Fe separation (>11 Å). In fact, the obtained value for J is larger than the coupling constants observed in μ-hydroxo-bridged di-iron(III) compounds and approaches the values for μ-oxo-bridged species.[37] This may suggest that there is some spin density on the phenyl ring of **2**, indicating a small contribution of the $[Fe^{II}\text{-tdt}^{\bullet}]^+$ resonance structure and providing an antiferromagnetic coupling pathway. However, $\pi-\pi$ stacking interactions in organic π radicals[38] or coordination compounds with π radical ligands[39,40] result in significantly larger coupling constants, although it has been shown that these are strongly dependent on the orientation of the π systems.[40,41]

The temperature dependence of the effective magnetic moment, μ_{eff}, of **3**(BF_4) (Figure 4 (bottom)) can be satisfactorily simulated using either a monomer or dimer model. In both cases, an average g_{av} value of 2.12, a χ_{TIP} of 497×10^{-6} emu, and a small amount of paramagnetic impurity of ~1% ($S = {}^5/_2$) were used to model the high-temperature plateau. The high-temperature limit of 1.93 μ_B for the monomer supports an $S = {}^1/_2$ ground state. The major difference between the two approaches is the simulation of the strong temperature-dependence of μ_{eff} in the region below 50 K. In the monomer model, this is achieved by assuming antiferromagnetic coupling to the continuum, resulting in a relatively large Weiss constant θ of -6.2 K. The second and potentially more physically accurate fit for the low-temperature region is again based on the observations from crystallography. For a dimer unit of antiferomagnetically coupled cations, a coupling constant J of -3.2 cm^{-1} is obtained from the fit. This implies that the efficiency of the antiferromagnetic exchange via hydrogen bonding in **3** is only 10% of the $\pi-\pi$ stacking pathway in **2**.

The X-band EPR spectra of **2** and **3** in frozen MeOH/toluene solution, shown in Figure 5, confirm the $S = {}^1/_2$ ground state of the molecules. Both spectra are rhombic with principal g values of 2.29, 2.18, and 1.96 for **2** and 2.21, 2.16, and 1.99 for **3**. The anisotropy of the g values in both compounds is too large for dithiolene radicals, but the data agree nicely with the values reported for similar Fe^{III} low-spin compounds.[4,42] However, the anisotropy in **3** ($\Delta g = 0.22$) is significantly lower than in **2** ($\Delta g = 0.33$). This indicates a higher contribution of the ligand to the SOMO induced by covalent bonding. As a result, the effective spin−orbit coupling constant is reduced, leading to lower g anisotropy. This parallels the trend observed by X-ray crystallography, where the smaller fold angle φ in **3** compared to that in **2** suggests stronger π interactions

(36) Hou, C.; Shi, J.-M.; Sun, Y.-M.; Shi, W.; Cheng, P.; Liu, L.-D. *J. Chem. Soc., Dalton Trans.* **2008**, 5970.

(37) (a) Gorun, S. M.; Lippard, S. J. *Inorg. Chem.* **1991**, *30*, 1625. (b) Weihe, H.; Güdel, H. U. *J. Am. Chem. Soc.* **1997**, *119*, 6539.

(38) Goto, K.; Kubo, T.; Yamamoto, K.; Nakasuji, K.; Sato, K.; Shiomi, D.; Takui, T.; Kubota, M.; Kobayashi, T.; Yakusi, K.; Ouyang, J. *J. Am. Chem. Soc.* **1999**, *121*, 1619.

(39) Koivisto, B. D.; Ichimura, A. S.; McDonald, R.; Lemaire, M. T.; Thompson, L. K.; Hicks, R. G. *J. Am. Chem. Soc.* **2006**, *128*, 690.

(40) Ren, X. M.; Nishihara, S.; Akutagawa, T.; Noro, S.; Nakamura, T. *Inorg. Chem.* **2006**, *45*, 2229.

(41) Norel, L.; Pointillart, F.; Train, C.; Chamoreau, L.-M.; Boubekeur, K.; Journaux, Y.; Brieger, A.; Brook, D. J. R. *Inorg. Chem.* **2008**, *47*, 2396.

(42) (a) Chun, H.; Verani, C. N.; Chaudhuri, P.; Bothe, E.; Bill, E.; Weyhermüller, T.; Wieghardt, K. *Inorg. Chem.* **2001**, *40*, 4157. (b) Higuchi, M.; Hitomi, Y.; Minami, H.; Tanaka, T.; Funabiki, T. *Inorg. Chem.* **2005**, *44*, 8810. (c) Girerd, J.-J.; Boillot, M.-L.; Blain, G.; Riviere, E. *Inorg. Chim. Acta* **2008**, *361*, 4012.

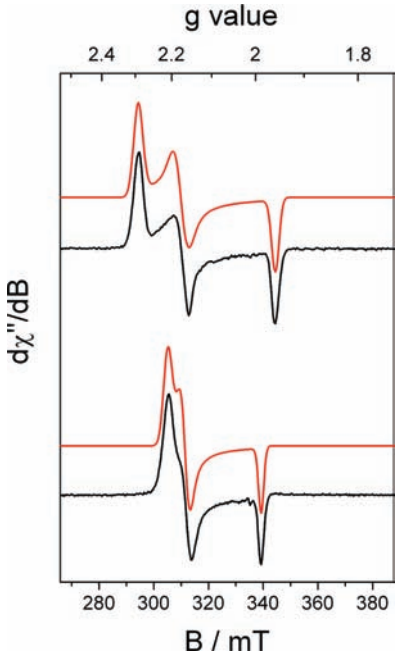

Figure 5. X-band EPR spectra of **2** (top) and **3** (bottom) recorded in a frozen MeOH/toluene solution at 10 K (frequency = 9.44 GHz, modulation = 0.7 mT, power = 0.02 mW). Simulated spectra are shown in red.

between metal and ligand. In other words, the contribution of the low-spin $[Fe^{II}$-dithiolene$^{\bullet}]^{+}$ resonance form is larger for **3** than for **2**.

The EPR spectrum of **1**, shown in Figure 6, is more complicated. It is dominated by a very intense signal at $g = 3.35$ corresponding to the g_{max} of the complex. Two g values, g_{mid} and g_{min}, are found at 1.77 and 0.80, respectively. Due to significant line broadening, g_{min} is almost not observable. The additional features observed in the region between $g = 2.5$ and $g = 1.9$ can be attributed to an $S = {}^1/_2$ impurity with g values of 2.45, 2.25, and 1.93. Although the signals of this impurity are quite prominent in the derivative spectrum, the total amount of impurity can be determined from the simulation to be only ~1%.

Due to the very large anisotropy of the g values, EPR spectra like the one observed for **1** are classified as highly anisotropic low-spin spectra.[43,44] These spectra are usually found and well-studied for the family of axially symmetric low-spin hemes[43] but have only recently been reported for nonheme compounds.[45] The spectrum confirms that complex **1** must be a low-spin ferric compound (d^5, $S = {}^1/_2$), like **2** and **3**. The exceptionally large anisotropy stems from an almost degenerate pair of orbitals in the t_{2g} set, yielding unusually large orbital contributions to the magnetic moment of the electron.

d. Spectroelectrochemistry. Cyclic voltammograms (CVs) of **1**−**3** have been recorded in either MeCN (for **1**$(OTf)_2 \cdot$MeCN and **3**$(BF)_4$) or CH_2Cl_2 (for **2**$(PF)_6$). [N-(n-Bu)$_4$]PF_6 was used as a supporting electrolyte (0.1 M) and a glassy carbon electrode as a working electrode. All potentials are referenced against the Fc^+/Fc couple using

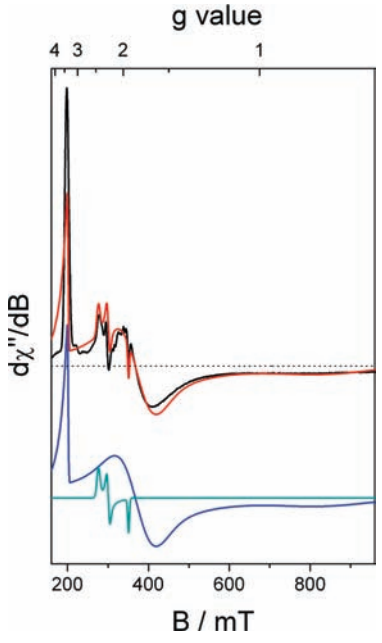

Figure 6. X-band EPR spectrum of **1** in frozen MeCN at 10.0 K (frequency = 9.45 GHz, modulation = 3.0 mT, power = 0.2 mW). The dashed line represents the baseline of the measurement. The simulated subspectrum for **1** is shown in blue, while the contribution from the impurity (~1%) is shown in green. The red line depicts the sum of the simulated subspectra.

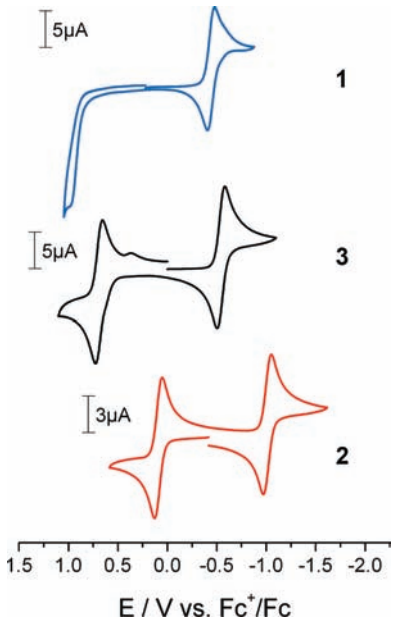

Figure 7. Cyclic voltammograms of **1** (blue), **3** (black), and **2** (red) in MeCN (**1** and **3**) and CH_2Cl_2 (**2**) at room temperature; 0.10 M [N(n-Bu)$_4$]-PF_6, scan rate 200 mV s^{-1}, glassy carbon working electrode.

ferrocene as an internal standard. The resulting CVs are shown in Figure 7, and the redox potentials are summarized in Table 3. All complexes show a reversible redox process, which was established to correspond to a one-electron reduction by controlled-potential coulometry. Since the starting materials **1**, **2**, and **3** contain completely reduced sulfur ligands, this reduction must be attributed to an iron-centered process ($Fe^{III} \rightarrow Fe^{II}$). Additionally, the two dithiolene compounds **2** and **3** display a second reversible process, which was shown to be a reversible

(43) (a) Migata, C.; Iwaizumi, M. *J. Am. Chem. Soc.* **1981**, *103*, 4378. (b) Salerno, J. C.; Leigh, J. S. *J. Am. Chem. Soc.* **1984**, *106*, 2156.

(44) Palmer, G. Electron Paramagnetic Resonance in Metalloproteins. In *Physical Methods in Bioinorganic Chemistry*; Que, L. Jr., Ed.; University Science Books: Sausalito, CA, 2000; pp 121−185.

(45) Duelund, L.; Toftlund, H. *Spectrochim. Acta, Part A* **2000**, *56*, 331.

Table 3. Redox Potentials in V vs Fc^+/Fc of Complexes[a]

complex	$E_{1/2}{}^1$	$E_{1/2}{}^2$	$\Delta(E_{1/2}{}^1 - E_{1/2}{}^2)$	ref
1		−0.44		this work
2	0.09	−1.01	1.10	this work
3	0.69	−0.54	1.18	this work
$[Fe^{III}(cyclam)(L_1{}^{ISQ\bullet})]^{2+}$	0.82	−0.63	1.45	30
$[Fe^{III}(cyclam)(L_2{}^{ISQ\bullet})]^{2+}$	0.73	−0.71	1.44	30
$[Fe^{III}(cyclam)(L_3{}^{ISQ\bullet})]^{2+}$	0.80	−0.42	1.22	30
$[Fe^{III}(L\text{-}N_4Me_2)(dbsq^\bullet)]^{2+}$	0.20			40

[a] Ligand abbreviations: $(L_1{}^{ISQ\bullet})^-$ = *o*-iminobenzosemiquinonate(1−); $(L_2{}^{ISQ\bullet})^-$ = 2-imino-4,6-di-*tert*-butylbenzosemiquinonate(1−); $(L_3{}^{ISQ\bullet})^-$ = *N*-phenyl-2-imino-4,6-di-*tert*-butylbenzosemi-quinonate(1−); $(dbsq^\bullet)^-$ = 3,5-di-*tert*-butylbenzosemiquinonate(1−); $L\text{-}N_4Me_2$ = *N*,*N*′-dimethyl-2,11-diaza[3.3]-(2,6)pyridinophane.

Scheme 2. Three-Membered Redox Series of **2**

$$[Fe^{II}(cyclam)(tdt)]^0 \underset{+e^-}{\overset{-e^-}{\rightleftharpoons}} [Fe^{III}(cyclam)(tdt)]^{1+} \underset{+e^-}{\overset{-e^-}{\rightleftharpoons}} [Fe^{III}(cyclam)(tdt^\bullet)]^{2+}$$

$S = 2$ $S = {}^1/_2$ $S = 0$

one-electron oxidation. This process is proposed to be ligand-centered, since it is absent in **1**, which contains the redox-innocent dithiocarbamate ligand. Instead, an additional irreversible oxidation peak is observed for **1** at ∼1.0 V, which was not investigated in further detail.

The three-membered redox series for **2** is shown in Scheme 2. Compared to **2**, the redox potentials in **3** are shifted to significantly higher potentials, while the separation between the two redox waves remains unchanged ($\Delta E \sim 1.1$ V). This effect can be explained by the different substituents on the dithiolene ligand. The strongly electron-withdrawing cyano groups of mnt^{2-} remove electron density from the dithiolene moiety, thus stabilizing the dianionic form of the ligand and decreasing its donor abilities.

The three-membered electron-transfer series of **2** and **3** were studied by controlled-potential coulometry at −25 °C, and the changes in the electronic absorption spectra were recorded. Figure 8 shows the spectra of **2**, its dicationic one-electron oxidized form $\mathbf{2}^{ox}$, as well as its neutral one-electron reduced form $\mathbf{2}^{red}$.

The monocation **2** shows two absorption bands above 400 nm with maxima at 580 nm (1020 M^{-1} cm^{-1}) and 825 nm (1910 M^{-1} cm^{-1}). On the basis of their high intensities, these bands are tentatively assigned as charge transfer bands. Upon reduction of **2** to $\mathbf{2}^{red}$, these bands diminish, though not to completeness due to the instability of $\mathbf{2}^{red}$ under the coulometry conditions. For the oxidized species $\mathbf{2}^{ox}$, three peaks are observed in the visible and NIR region (443 nm (1950 M^{-1} cm^{-1}), 592 nm (4400 M^{-1} cm^{-1}), and 824 nm (860 M^{-1} cm^{-1})). The spectrum is dominated by an intense band at 592 nm, which is clearly a charge-transfer transition. However, on the basis of this transition, it is not possible to distinguish between a ligand-centered oxidation, yielding $[Fe^{III}(cyclam)(tdt^\bullet)]^{2+}$, or a metal-centered process, yielding $[Fe^{IV}(cyclam)(tdt)]^{2+}$. The electronic absorption spectra of the three-membered redox series for **3** show similar features in the visible region, but the intensities of the bands are half of those observed for **2**. A number of additional bands can be found below 400 nm, which are probably due to low-lying ligand π^* orbitals. This is most noticeable in $\mathbf{3}^{red}$, which shows

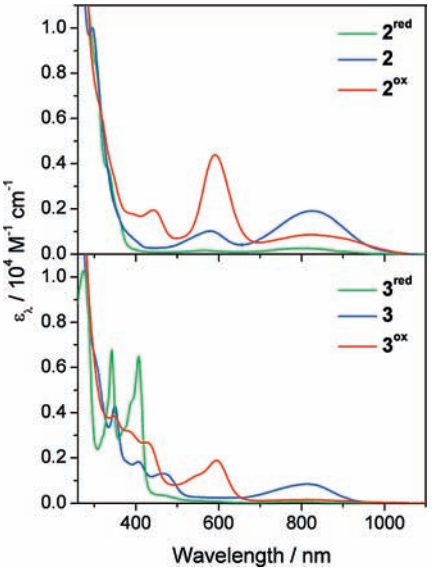

Figure 8. Electronic absorption spectra of **2** (blue) and its electrochemically generated oxidized and reduced form, $\mathbf{2}^{ox}$ (red) and $\mathbf{2}^{red}$ (green), in CH_2Cl_2 at −25 °C (top). Electronic absorption spectra for the three-membered redox series of **3** in MeCN at −25 °C (bottom).

Table 4. Zero-field Mössbauer Parameters for Solid Samples of **1**, **2**, **3**, and Frozen Acetonitrile Solutions of Electrochemically Generated $\mathbf{2}^{ox}$ and $\mathbf{2}^{red}$ at 80 K[a]

complex	isomer shift δ, mm s^{-1} [b]	quadrupole splitting ΔE_Q, mm s^{-1}
1	0.35 (0.39)	1.52[c] (+2.27)
2	0.38 (0.41)	1.80[c] (+1.95)
$\mathbf{2}^{ox}$	0.29 (0.36)	−2.24 (−2.47)
$\mathbf{2}^{red}$	1.00 (0.86)	3.55[c] (+3.88)
3	0.33 (0.40)	1.96[c] (−2.11)
$[Fe^{III}(cyclam)(L_3{}^{ISQ\bullet})]^{2+}$ [d]	0.33	1.88[c]
$[Fe^{III}(L\text{-}N_4Me_2)(dbsq^\bullet)]^{2+}$ [e]	0.18	2.32[c]

[a] Calculated parameters are given in parentheses. [b] Relative to α-Fe at 298 K. [c] The sign has not been determined experimentally. [d] Ref 30. [e] Data at 4.2 K; ref 40.

two intense bands (407 nm (6770 M^{-1} cm^{-1}) and 342 nm (6480 M^{-1} cm^{-1})) with additional shoulders in this region.

e. Mössbauer Spectroscopy. Zero-field Mössbauer spectra of solid samples of $\mathbf{1}(OTf)_2 \cdot MeCN$, $\mathbf{2}(PF_6)$, and $\mathbf{3}(BF_4)$ have been recorded at 80 K; the results are summarized in Table 4. Interestingly, the isomer shifts δ of **1**, **2**, and **3** are observed in the narrow range of 0.33−0.38 mm s^{-1}, and the quadrupole splitting parameters are also quite similar (1.52−1.96 mm s^{-1}). These data are compatible with other octahedral low-spin ferric complexes.[4,30,46]

To gain a better understanding of the electronic structure of $\mathbf{2}^{red}$ and $\mathbf{2}^{ox}$, Mössbauer measurements were conducted on frozen solutions of these electrochemically generated complexes. Since Mössbauer spectroscopy is a very sensitive probe for the electronic environment around the iron nucleus, an unambiguous analysis of the oxidation state is possible in comparison to the established oxidation state of the starting material **2**. Therefore, the coulometric experiments were repeated

(46) Koch, W. O.; Schünemann, V.; Gerdan, M.; Trautwein, A. X.; Krüger, H.-J. *Chem. Eur. J.* **1998**, *4*, 1255.

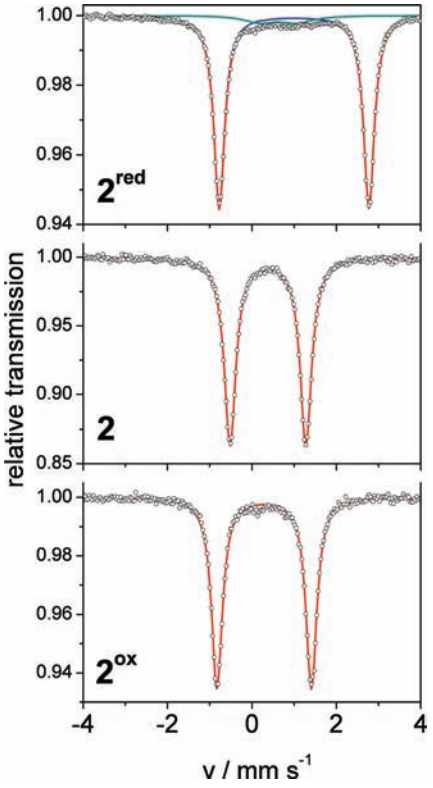

Figure 9. Zero-field Mössbauer spectra of **2** and the electrochemically generated species $\mathbf{2}^{ox}$ and $\mathbf{2}^{red}$ in MeCN (3 mM, 80 K). Simulations are shown in red. The spectrum of $\mathbf{2}^{red}$ contains 3% of an unidentified impurity, shown in green.

with an ^{57}Fe-enriched sample of **2** in MeCN. The resulting spectra are shown in Figure 9, and the Mössbauer parameters are also summarized in Table 4.

As has been established earlier, **2** contains a low-spin ferric ion, which is in good agreement with the observed isomer shift δ of 0.38 mm s^{-1} and a quadrupole splitting ΔE_Q of 1.80 mm s^{-1}. Upon reduction to $\mathbf{2}^{red}$, a different spectrum is obtained, corroborating that the reduction is a metal-centered process ($Fe^{III} \rightarrow Fe^{II}$). Interestingly, the spin state of the iron ion changes from low-spin ferric (d^5) to high-spin ferrous (d^6), which is unequivocally established by the very large values for δ and ΔE_Q. This is different from the isoelectronic species $[Co^{III}(tren)(bdt)]^+$ (bdt^{2-} = benzene-1,2-dithiolate(2−)),[1] which also possesses a d^6 metal ion coordinated to a closed-shell dithiolene, but the central metal ion remains in a low-spin state.

The oxidized species $\mathbf{2}^{ox}$ shows very similar values for δ and ΔE_Q as compared to those observed for **2**. This indicates that the oxidation level and spin state of the iron ion are unchanged upon oxidation, which implies a ligand-centered oxidation that leaves the iron ion as low-spin ferric. For a metal-centered oxidation, typical changes in the isomer shift of 0.15−0.25 mm s^{-1} would be observed.[47] Nevertheless, the change of $\Delta\delta = 0.09$ mm s^{-1} going from **2** to $\mathbf{2}^{ox}$ is larger than in the corresponding imidophenolate series.[30] As will be shown by DFT calculations below, this effect is attributed to a decrease in the fold angle φ upon oxidation. Consequently, the Mössbauer spectra support the electronic structure description of $[Fe^{III}(cyclam)(tdt^{\bullet})]^{2+}$ for $\mathbf{2}^{ox}$.

(47) Berry, J. F.; Bill, E.; Bothe, E.; DeBeer George, S.; Mienert, B.; Neese, F.; Wieghardt, K. *Science* **2006**, *312*, 1937.

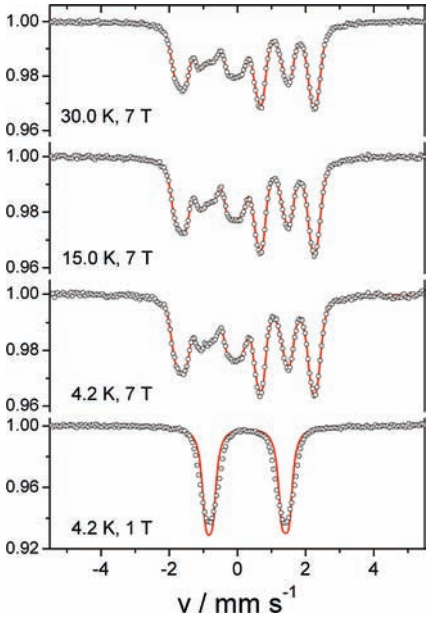

Figure 10. Applied-field Mössbauer spectra of electrochemically generated $\mathbf{2}^{ox}$ in MeCN (3 mM) with variable temperature (4.2, 15.0, and 30.0 K) and fields (1 and 7 T). The fits are shown as red lines, with δ (ΔE_Q) = 0.29 (−2.24) mm s^{-1}. Other fitting parameters are as follows: asymmetry parameter η = 0.56; S = 0; line width = 0.23 mm s^{-1}.

Further confirmation is retrieved from applied-field Mössbauer measurements carried out on $\mathbf{2}^{ox}$ at 1 and 7 T (Figure 10). The temperature independence of the spectra (4.2−30 K) in high field at 7 T is a clear indication of the absence of an internal magnetic field around the iron nucleus. Therefore, $\mathbf{2}^{ox}$ must possess a diamagnetic ground state ($S = 0$). Indeed, all spectra can be fitted with the same set of parameters by assuming an $S = 0$ spin state and by using the parameters δ and ΔE_Q from the zero-field measurements. Additionally, the sign of the quadrupole splitting was obtained from the simulation, giving a ΔE_Q value of −2.24 mm s^{-1}. In an octahedral ligand field, the $S = 0$ ground state can only result from an antiferromagnetic coupling between the low-spin iron(III) center with a ligand radical. The Fe^{IV} alternative has an $S = 1$ ground state, because for a first row transition metal the splitting within the t_{2g} set is too small to allow an $S = 0$ low-spin configuration.

f. X-Ray Absorption Spectroscopy. Metal K-edge XAS is a powerful local probe of the geometric and electronic structure of the central metal ion in coordination compounds and can be used as an indicator of the metal oxidation state.[48] For first row transition metals, an increase of ∼1 eV per oxidation state is typical.[47,49] Figure 11 compares the Fe K-edge spectra of **1**, **2**, and $\mathbf{2}^{ox}$.

Since **1** has been unambiguously assigned to contain a low-spin ferric ion, it can be used as a reference for Fe^{III} in octahedral *cis*-N_4S_2 coordination. The rising edge position is almost identical in all three compounds, giving the first indication for a constant +III oxidation state in the

(48) (a) DuBois, J. L.; Mukherjee, P.; Stack, T. D. P.; Hedman, B.; Solomon, E. I.; Hodgson, K. O. *J. Am. Chem. Soc.* **2000**, *122*, 5775. (b) Westre, T. E.; Kennepohl, P.; DeWitt, J. G.; Hedman, B.; Hodgson, K. O.; Solomon, E. I. *J. Am. Chem. Soc.* **1997**, *119*, 6297.

(49) Kapre, R. R.; Ray, K.; Sylvestre, I.; Weyhermüller, T.; DeBeer George, S.; Neese, F.; Wieghardt, K. *Inorg. Chem.* **2006**, *45*, 3499.

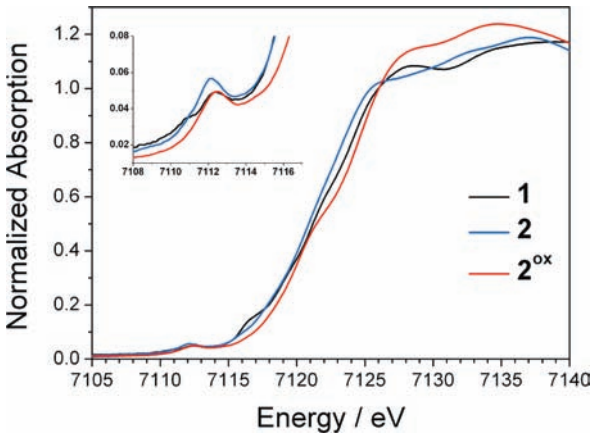

Figure 11. Normalized Fe K-edge X-ray absorption spectra of **1** (black), **2** (blue), and $\mathbf{2^{ox}}$ (red). The inset is an expansion of the pre-edge region.

three complexes. The additional, low-intensity shoulder in the rising edge at 7116.5 eV for **1** may be attributed to a charge-transfer (shakedown) transition. However, the pre-edge energy (resulting from electric-dipole-forbidden 1s → 3d transitions) is a clearer indicator of the oxidation state. Reference complex **1** shows a main peak at 7112.4 eV and a shoulder at 7111.0 eV. One pre-edge feature is observed at 7112.2 eV in **2**. The very similar pre-edge energy for **2** as compared to **1** confirms that the central Fe ion in **2** also possesses a +III oxidation state, supporting the previous conclusions from EPR spectroscopy. Upon oxidation, the spectrum remains almost unchanged, showing a pre-edge transition at 7112.5 eV for $\mathbf{2^{ox}}$. The observed pre-edge shift of 0.3 eV is much smaller than 1 eV. This indicates that the oxidation is not a metal-centered process but ligand-centered, in agreement with the results from electrochemistry and Mössbauer spectroscopy. In summary, the Fe K-edge XAS data confirm the low-spin Fe^{III} description for $\mathbf{2^{ox}}$.

The sulfur K-edge results from an electric dipole-allowed local 1s → 4p transition.[50] In cases where the ligand is bound to a transition metal with a partially filled d shell, the covalent interaction between the ligand 3p orbitals and the metal 3d orbitals produces partial-ligand 3p hole character, resulting in a pre-edge transition, the intensity of which will reflect the covalency of the metal−ligand bond.[50,51] Furthermore, the energy of the pre-edge transition is affected by the energy of the unoccupied (or partially occupied) 3d orbitals (which will have contributions from the ligand field and effective nuclear charge (Z_{eff})) and the energy of the ligand 1s core.

The S K-edge XAS spectra of **2**, $\mathbf{2^{ox}}$, and $[Co^{III}(tren)(bdt)]^+$, **4**,[1] are shown in Figure 12. Complex **4** represents a reference for a complex with a dianionic, closed-shell dithiolene ligand coordinated to a diamagnetic, octahedral low-spin transition metal ion with a filled t_{2g} set (d^6). The formally isoelectronic Fe(II) complex $\mathbf{2^{red}}$ cannot serve as a reference, since it has been shown to contain a high-spin ferrous ion (see above). The electric-dipole-allowed edge feature is found at 2473.5 and 2473.6 eV

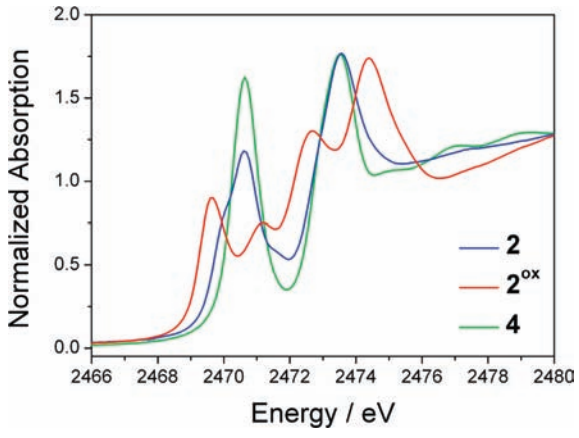

Figure 12. Comparison of the normalized S K-edge spectra of **2**, $\mathbf{2^{ox}}$, and $[Co^{III}(tren)(bdt)]^{2+}$ (**4**).

for **4** and **2**, respectively, in agreement with a closed-shell dianionic dithiolene ligand for both compounds. Upon oxidation to $\mathbf{2^{ox}}$, this feature shifts to 2474.4 eV, indicating a ligand-centered redox process resulting in a ligand π radical for $\mathbf{2^{ox}}$. Since the S 1s orbital is much more exposed to Z_{eff} than the more effectively shielded S 4p orbitals, the increase in Z_{eff} upon oxidation of the ligand stabilizes the 1s orbital more strongly and, consequently, increases the transition energy. The edge feature in $\mathbf{2^{ox}}$ is shifted to remarkably high energy even when compared to other radical-containing complexes.[52,53] This is most likely due to the fact that the radical in $\mathbf{2^{ox}}$ cannot be delocalized over multiple noninnocent ligands.

The dramatic changes in the pre-edge region of the spectra are further proof of a change in the electronic structure of the ligand upon oxidation from **2** to $\mathbf{2^{ox}}$. The deconvoluted S K-edge spectra of **2**, $\mathbf{2^{ox}}$, and **4** and the second derivative spectra of the experimental data are shown in Figure 13. The spectrum of the reference compound **4** shows only one feature at 2470.6 eV in the pre-edge region (2468−2473 eV), which can be attributed to transitions into the almost degenerate σ-antibonding e_g orbitals (d_{xy} and d_{z^2}, Co−S σ^*). The intensity of the peak (shown in blue) indicates high ligand−metal covalency. Further inspection of the second derivative spectrum clearly reveals a second band at 2472.8 eV (shown in orange), which is buried in the edge feature. This peak results most likely from transitions into the empty ligand π^* orbitals.

The same feature can also be found as a shoulder in the edge feature of the S K-edge spectrum of **2** (2472.8 eV) and is again more clearly identified in the second derivative spectrum. Furthermore, three additional pre-edge features are observed for **2** between 2468 and 2472 eV. The lowest peak at 2470.0 eV (shown in red) can be attributed to a transition to the t_{2g} SOMO of **2**, which gains intensity by weak covalent interaction between the metal d_{xz} orbital and the π-donor orbital of the ligand and, therefore, indicates a small contribution of the $[Fe^{II}\text{-}tdt^{\bullet}]^+$ resonance structure. As will be shown in the computational part of this work (see below), the two

(50) (a) Glaser, T.; Hedman, B.; Hodgson, K. O.; Solomon, E. I. *Acc. Chem. Res.* **2000**, *33*, 859. (b) Solomon, E. I.; Hedman, B.; Hodgson, K. O.; Dey, A.; Szilagyi, R. K. *Coord. Chem. Rev.* **2005**, *249*, 97.
(51) Neese, F.; Hedman, B.; Hodgson, K. O.; Solomon, E. I. *Inorg. Chem.* **1999**, *38*, 4854.
(52) Pap, J. S.; Benedito, F. L.; Bothe, E.; Bill, E.; DeBeer George, S.; Weyhermüller, T.; Wieghardt, K. *Inorg. Chem.* **2007**, *46*, 4187–4191.
(53) Ray, K.; DeBeer George, S.; Solomon, E. I.; Wieghardt, K.; Neese, F. *Chem. Eur. J.* **2007**, *13*, 2783.

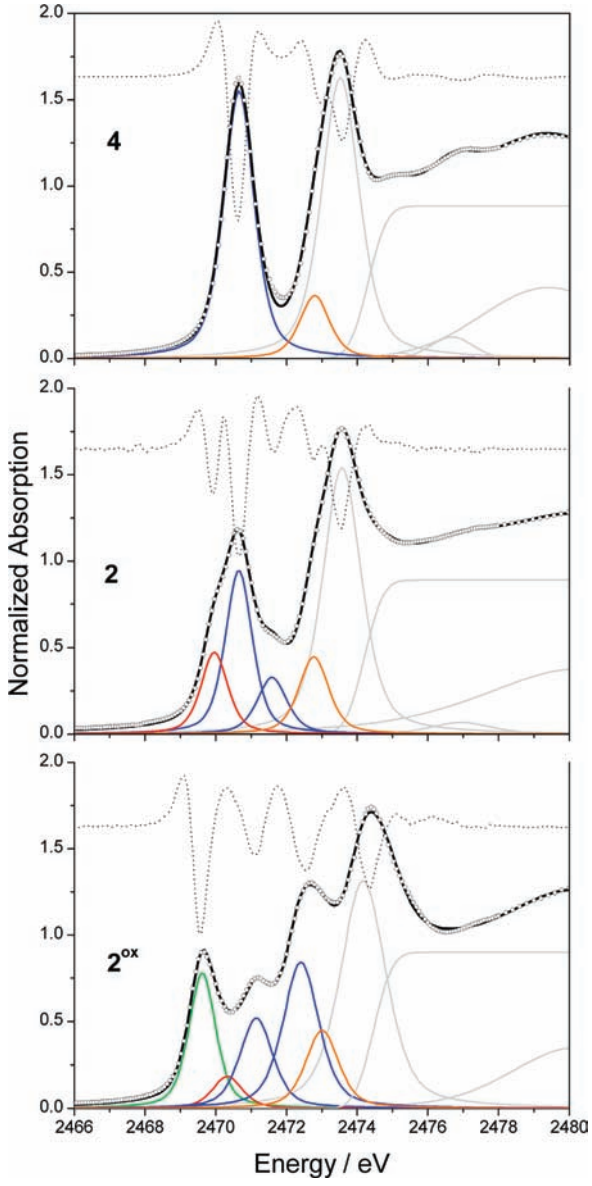

Figure 13. Pseudo-Voigt fits to the S K-edge XAS data of **4**, **2**, and $\mathbf{2^{ox}}$ (green (S 1s→ $L_{\pi^*}{}^{\bullet}$), red (S 1s→ t_{2g}), blue (S 1s→ e_g), orange (S 1s→ L_{π^*}), and gray; see text for details). The sum of the peaks is shown as the black line, and the dotted line represents the second derivative of the experimental spectrum.

remaining peaks at 2470.6 and 2471.6 eV (shown in blue) are due to transitions to the σ-antibonding e_g orbitals (Fe−S σ^*), which are split by significant multiplet effects[54] that have previously not been reported for S K-edge spectra. However, multiplet splittings have recently been reported for the Fe K-edge spectra of a series of oxo-Fe(IV) complexes.[55] The observed multiplet splitting of 1.0 eV is testimony of the paramagnetic ($S = {}^1/_2$) low-spin ferric center in **2**.

The spectrum of $\mathbf{2^{ox}}$ shows three clearly resolved pre-edge features, with maxima at 2469.6, 2471.1, and 2472.6 eV. However, a thorough analysis of the second derivative spectrum in combination with the computational results (see below) suggests the presence of two more features in the spectrum. A peak at 2473.0 eV (shown in orange) becomes apparent from a shoulder in the second derivative spectrum. Its position and intensity allow the tentative assignment as transitions to the ligand π^* orbitals already observed in **2** and **4**. Due to the higher oxidation level of the dithiolene ligand in $\mathbf{2^{ox}}$, these transitions are shifted to slightly higher energies. The second, more ambiguous feature at 2470.3 eV (shown in red) is barely visible even in the second derivative spectrum, but its inclusion in the deconvolution of the spectrum improved the fit significantly. Even though the assignment from the derivative spectrum is quite speculative, it is supported by the computational results (see below), and the feature accounts nicely for the transition to a half-filled d_{xz} orbital. The lowest-energy peak at 2469.6 eV (shown in green), absent in **2**, is due to the ligand radical in $\mathbf{2^{ox}}$. The peak position is in good agreement with the observed transitions in previously reported radical species.[53,56] The two remaining transitions at 2471.1 and 2472.4 eV (shown in blue) can again be assigned as transitions to the empty iron e_g orbitals, which are again split by multiplet effects (1.3 eV). A more detailed analysis of the transitions and the multiplet effects is presented in the theoretical section (see below).

g. DFT Calculations. The ground-state geometries of **1**−**3** and their redox isomers have been optimized by using the B3LYP functional. For **2** and the related compounds $\mathbf{2^{red}}$ and $\mathbf{2^{ox}}$, the methyl group of the tdt^{2-} ligand was replaced by a proton. Spin-unrestricted DFT methods were applied for **1**, **2**, and **3** to account for the experimentally determined $S = {}^1/_2$ ground state. As shown in Table 5, the agreement of the structural parameters between experiment and calculation is excellent. The intraligand bond distances agree within ±0.02 Å, whereas the Fe−S and Fe−N bond distances are overestimated by up to 0.08 Å, which is typical for the B3LYP functional. Note that the trend in the fold angle φ is well-reproduced for **2** and **3**, even though the calculations were started with $\varphi = 0$.

For the oxidized complexes $\mathbf{2^{ox}}$ and $\mathbf{3^{ox}}$, a broken symmetry BS(1,1) $M_S = 0$ model was assumed, as well as a simple closed-shell spin-restricted $S = 0$ approach. In both cases, the broken symmetry solution was significantly lower in energy (6.8 kcal mol^{-1} and 7.5 kcal mol^{-1}, respectively), confirming the singlet diradical character of these species.[57] The reduced species $\mathbf{2^{red}}$ was calculated assuming an $S = 2$ ground state, in agreement with the high-spin ferrous assignment based on Mössbauer spectroscopy.

The calculated electronic structure of **1** is in agreement with a d^5 low-spin ferric description. The spin density plot obtained from a Mulliken population analysis is shown in Figure 14. The positive spin density of 1.21 indicates a single unpaired electron on the iron, which is overestimated by spin polarization of the σ bonds. This can also be seen from the small amount of negative spin density on

(54) (a) Fadley, C. S.; Shirley, D. A.; Freeman, A. J.; Bagus, P. S.; Mallow, J. V. *Phys. Rev. Lett.* **1969**, *23*, 1397. (b) de Groot, F. *Coord. Chem. Rev.* **2005**, *249*, 31.

(55) Berry, J. F.; DeBeer George, S.; Neese, F. *Phys. Chem. Chem. Phys.* **2008**, *10*, 4361.

(56) (a) Kapre, R. R.; Bothe, E.; Weyhermüller, T.; DeBeer George, S.; Muresan, N.; Wieghardt, K. *Inorg. Chem.* **2007**, *46*, 7827. (b) Kapre, R. R.; Bothe, E.; Weyhermüller, T.; DeBeer George, S.; Wieghardt, K. *Inorg. Chem.* **2007**, *46*, 5642. (c) Szilagyi, R. K.; Lim, B. S.; Glaser, T.; Holm, R. H.; Hedman, B.; Hodgson, K. O.; Solomon, E. I. *J. Am. Chem. Soc.* **2003**, *125*, 9158.

(57) Bachler, V.; Olbrich, G.; Neese, F.; Wieghardt, K. *Inorg. Chem.* **2002**, *41*, 4179–4193.

Table 5. Comparison of Experimental and Calculated Bond Distances (Å) and Folding Angles φ (deg) for **1**−**3**, $\mathbf{2}^{red}$, $\mathbf{2}^{ox}$, and $\mathbf{3}^{ox}$

	1			$\mathbf{2}^{red}$	**2**		$\mathbf{2}^{ox}$		**3**		$\mathbf{3}^{ox}$
	exptl	calcd		calcd	exptl	calcd	calcd		exptl	calcd	calcd
Fe(1) − N(1)	2.0302(11)	2.074	Fe(1) − N(5)	2.266	1.985(5)	2.084	2.082	Fe(1) − N(5)	2.0335(11)	2.086	2.086
Fe(1) − N(5)	2.0509(11)	2.099	Fe(1) − N(1)	2.392	2.102(3)	2.139	2.116	Fe(1) − N(1)	2.0855(10)	2.133	2.108
Fe(1) − N(12)	2.0480(10)	2.097	Fe(1) − N(8)	2.394	2.064(7)	2.141	2.116	Fe(1) − N(8)	2.0646(11)	2.133	2.107
Fe(1) − N(8)	2.0339(11)	2.073	Fe(1) − N(12)	2.265	2.088(5)	2.078	2.085	Fe(1) − N(12)	2.0463(11)	2.085	2.086
Fe(1) − S(21)	2.2902(3)	2.337	Fe(1) − S(21)	2.394	2.2361(6)	2.265	2.295	Fe(1) − S(24)	2.2337(4)	2.270	2.302
Fe(1) − S(23)	2.2909(3)	2.339	Fe(1) − S(28)	2.394	2.2411(7)	2.274	2.293	Fe(1) − S(21)	2.2447(3)	2.267	2.302
S(21) − C(22)	1.7274(13)	1.748	S(21) − C(22)	1.788	1.754(2)	1.773	1.727	S(24) − C(23)	1.7278(12)	1.758	1.711
S(23) − C(22)	1.7296(12)	1.746	S(28) − C(27)	1.788	1.750(2)	1.774	1.727	S(21) − C(22)	1.7296(13)	1.758	1.711
C(22) − N(24)	1.3171(15)	1.315	C(22) − C(23)	1.409	1.403(3)	1.408	1.419	C(23) − C(22)	1.3666(17)	1.374	1.421
			C(23) − C(24)	1.396	1.387(3)	1.394	1.381				
			C(24) − C(25)	1.400	1.378(4)	1.405	1.428				
			C(25) − C(26)	1.396	1.384(4)	1.394	1.381				
			C(26) − C(27)	1.409	1.401(3)	1.408	1.419				
			C(27) − C(22)	1.421	1.391(3)	1.411	1.445				
			φ	0.34	33.03	20.21	1.86	φ	9.53	3.67	0.72

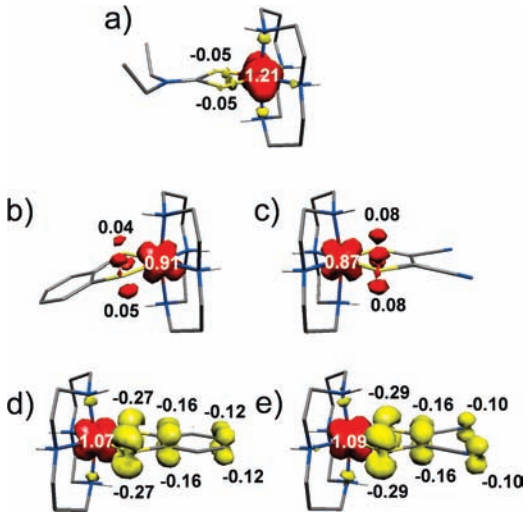

Figure 14. Mulliken spin density plots for (a) **1**, (b) **2**, (c) **3**, (d) $\mathbf{2}^{ox}$, and (e) $\mathbf{3}^{ox}$ (red, α-spin density; yellow, β-spin density).

the ligands, which resides exclusively in σ-type orbitals. The unpaired electron in **1** is located in a metal-d orbital that is a linear combination of the d_{yz} (70%) and $d_{x^2-y^2}$ (24%) orbitals.

For **2** and **3**, the calculations support the low-spin $[Fe^{III}(tdt^{2-})]^+$ and $[Fe^{III}(mnt^{2-})]^+$ description, respectively. The optimized structures show long C−S bonds of 1.774 Å and 1.758 Å, respectively, reproducing the shorter C−S bonds for mnt^{2-}. In addition, two doubly occupied metal orbitals (d_{yz} and $d_{x^2-y^2}$), two empty metal orbitals (d_{xy} and d_{z^2}), and a predominantly metal-centered SOMO (d_{xz}) can be found in the orbital manifolds of **2** and **3**. Accordingly, the Mulliken spin density plots shown in Figure 14 indicate one unpaired electron on the iron center, which resides predominantly in the d_{xz} orbital for both complexes. Only a small amount of spin density is transferred to the ligand, indicating weak covalent π interactions. Remarkably, the amount of delocalization is higher in **3**, which agrees nicely with the lower anisotropy observed in the *g* values of this compound. Furthermore, this parallels the trend in the fold angle φ, which decreases for **3** compared to **2** due to stronger π interaction.

Upon oxidation to $\mathbf{2}^{ox}$ and $\mathbf{3}^{ox}$, the metal orbital manifold remains almost unchanged (low-spin d^5). but one electron is removed from the ligand. This is nicely represented by the spin density plots shown in Figure 14. One unpaired electron with α spin is found on the iron center, whereas one electron with β spin is delocalized over the ligand, with major contributions from the sulfur atoms. Note that the spin density distribution of a broken symmetry singlet calculation is nonphysical, because in a genuine singlet state the spin density has to be zero at any point in space. It is therefore clear that the BS formalism only crudely models the multireference character of these species, but is not an entirely satisfactorily substitute for a multiconfigurational treatment.[58] Nevertheless, the spin density plots shown in Figure 14 are a practical representation of the diradical character of $\mathbf{2}^{ox}$ and $\mathbf{3}^{ox}$. The C−S bond lengths of 1.727 and 1.711 Å in $\mathbf{2}^{ox}$ and $\mathbf{3}^{ox}$, respectively, are significantly shorter than those in **2** and **3**, and the aromatic ring in $\mathbf{2}^{ox}$ shows a quinoidal-type distortion. These structural features are typical for the monoanionic radical form of dithiolene ligands. The magnetic orbitals[22] of $\mathbf{2}^{ox}$ are shown in Figure 15. The overlap between these two orbitals provides an antiferromagnetic exchange coupling pathway that gives rise to the diamagnetic ground state and forces the ligand into a planar arrangement ($\varphi = 0°$).

In order to calibrate the electronic structures shown above, Mössbauer parameters were calculated (Table 4).[24,25] For all investigated complexes, the calculated parameters are in excellent agreement with the experiment, supporting the accuracy of the calculated electronic structures. For the isomer shift δ, deviations of ±0.1 mm s^{-1} are acceptable. Reassuringly, the calculations also reproduce the change in the isomer shift upon oxidation of **2** to $\mathbf{2}^{ox}$. On the basis of the optimized structures, this can now clearly be attributed to a change in φ, from 20.21° in **2** to 1.86° in $\mathbf{2}^{ox}$.

h. Time-Dependent DFT Calculations. In order to obtain a deeper understanding of the pre-edge transitions in S and Fe K-edge X-ray absorption spectroscopy, time-dependent DFT (TD-DFT) calculations were conducted for **2** and $\mathbf{2}^{ox}$ at the BP86 and B3LYP levels of theory. A simple protocol for the direct calculation of pre-edge spectra has been developed recently.[26,53] Due to the limitations in the accurate treatment of excited states in

(58) Herebian, D.; Wieghardt, K.; Neese, F. *J. Am. Chem. Soc.* **2003**, *125*, 10997.

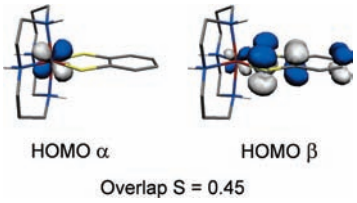

Figure 15. Magnetic orbitals of $\mathbf{2^{ox}}$.

DFT, *absolute* transition energies cannot be obtained by this method. Nevertheless, the *relative* transition energies and the *relative* intensities are, in general, reliably modeled. For a given theoretical method, that is, combination of functional, basis sets, relativistic treatment, and so forth, an empirical correction factor for energy and intensity can be introduced. The specific corrections for the calculations presented in this work are given in the Experimental Section.

However, the computations are further complicated for systems with open-shell transition metal ions due to the presence of multiplet effects. These are the result of shell-opening excitations from the 1s core orbitals into empty d orbitals, thus creating configurations with several unpaired electrons. Such a configuration creates multiple linearly independent states. In a spin-unrestricted TD-DFT calculation, however, there are only two determinants that arise from the excitation of either an α-spin or a β-spin core electron. Their energy difference arising from spin-polarization is, therefore, only a crude estimate of the multiplet splitting arising from the final-state configuration. Consequently, the errors in the calculation of energies and intensities of such multiplet split transitions are expected to be larger than typically observed for systems with diamagnetic transition metal centers. Unfortunately, a more satisfactory solution to the multiplet problem on the basis of TD-DFT is currently not possible. We found that, when the BP86 functional is used, the calculated splittings reflect merely the spin polarization of the acceptor orbitals in the ground-state electronic structure. However, when the B3LYP functional is used, the resulting splittings are deviating from the spin polarization of the ground state and agree much better with the experimentally observed values. This is due to the inclusion of exact Hartree−Fock exchange in the excited-state calculations using the hybrid functional B3LYP. A comparison of the TD-DFT calculations for **2** using BP86 or B3LYP is shown in Figure S2 (Supporting Information). In the following, only the results from the B3LYP calculations will be discussed.

A comparison of the calculated and experimental S K-pre-edge spectra is shown in Figure 16, and important transitions are summarized in Table 6. The assignment of the peaks is based on the acceptor orbitals, which contribute most to the computed transition. For **2**, the experimental spectrum is reproduced with excellent agreement in the relative peak positions. Five transitions are observed in the pre-edge region. The first calculated transition at 2470.0 eV corresponds to the excitation of an S 1s electron with β spin into the SOMO of **2**, which is predominantly metal-centered (56.5% d_{xz}, 12.7% $d_{x^2-y^2}$), with some sulfur p_z character (18.1%). As expected, the transitions to the almost degenerate e_g set (d_{z^2} and d_{xy}) show significant

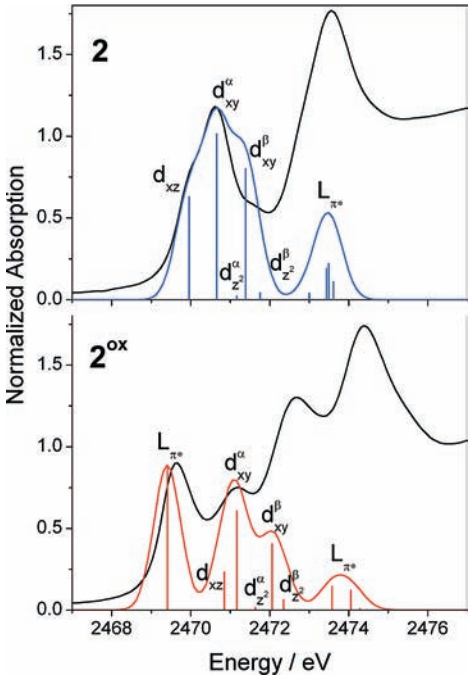

Figure 16. Comparison of the calculated (blue and red) and experimental (black) S K-edge XAS spectra of **2** (top) and $\mathbf{2^{ox}}$ (bottom). The calculated transitions are represented by the stick plots. The labels represent the acceptor orbitals with the highest contribution to the corresponding transition. A line broadening of 0.8 eV was assumed for the calculated spectra.

multiplet splitting. The α-spin transitions are computed to occur at 2470.6 and 2471.2 eV for d_{xy} and d_{z^2}, respectively. Since the d_{xy} orbital is σ-bonding with respect to the dithiolene ligand, a high S 3p contribution is found (29.1%), yielding a large intensity for the transition. Only very weak interactions between the dithiolene and the torus of the d_{z^2} orbital are possible. Therefore, the sulfur content of the orbital (6.7%) and the intensity of the transition are low. The same intensity pattern is found for the β-spin transitions, which are computed to occur at 2471.4 and 2471.8 eV for d_{xy} and d_{z^2}, respectively. The magnitude of the multiplet splitting is slightly underestimated by TD-DFT, giving a theoretical value of 0.8 and 0.6 eV for d_{xy} and d_{z^2}, respectively, versus an experimental splitting of 1.0 eV. It is, however, larger than the spin polarization of the ground-state d_{xy} and d_{z^2} orbitals ($\Delta E_{\alpha-\beta}$ = 0.6 eV). Several transitions to the ligand π^* orbitals are predicted between 2473.0 and 2473.6 eV in reasonable agreement with the experimental data. The transition energy is slightly overestimated.

The calculated spectrum of $\mathbf{2^{ox}}$ is more problematic. Due to its open-shell singlet character, even the ground state cannot be adequately described by a single determinantal framework. Consequently, a linear response treatment for TD-DFT based on an inadequate ground state cannot be expected to yield reasonable quantitative results for the electronically excited states for which the intricate problems related to multideterminantal character are amplified.[53] Nevertheless, a qualitative description was attempted. The BS TD-DFT calculated spectrum of $\mathbf{2^{ox}}$, as shown in Figure 16, exhibits three resolved pre-edge features, which originate from six transitions. The lowest-energy feature is due to a single transition into the

Table 6. Calculated and Experimentally Observed Transitions in the S K Pre-Edge and Fe K Pre-Edge Spectra of **2** and $\mathbf{2^{ox}}$

2				
		S K-edge		Fe K-edge
		exptl/eV	calcd/eV	calcd/eV
L π* (radical)				
d_{xz}		2470.0	2470.3	7111.0
d_{xy}	α	2470.6	2470.6	7112.3
	β	2471.6	2471.4	7112.5
d_{z^2}	α		2471.2	7111.5
	β		2471.8	7111.9
L π*		2472.8	2473.0−2473.6	
$\mathbf{2^{ox}}$				
		S K-edge		Fe K-edge
		exptl/eV	calcd/eV	calcd/eV
L π* (radical)		2469.6	2469.4	7114.4
d_{xz}		2470.3	2470.8	7110.8
d_{xy}	α	2471.1	2471.2	7112.4
	β	2472.4	2472.1	7112.6
d_{z^2}	α		2471.6	7111.8
	β		2472.4	7112.1
L π*		2473.0	2473.6−2474.4	

half-filled β-SOMO of the ligand radical (π*) at 2469.4 eV. This orbital is centered almost exclusively on the ligand and possesses very high sulfur (45.4%) character, generating a very intense peak. The next band at 2470.8 eV stems from a transition into the metal d_{xz} orbital (α-SOMO). Its low intensity is derived from the overlap of the magnetic orbitals causing the antiferromagnetic coupling (10.2% S p_z character). Similar to the experiment, this transition is not resolved in the calculated spectrum, assuming a 0.8 eV line broadening.

The subsequent four transitions result from excitations into the vacant metal e_g orbitals. In analogy to complex **2**, these transitions are split due to multiplet effects. The α-spin transitions are computed at 2471.2 and 2471.6 eV for d_{xy} and d_{z^2}, respectively, while the corresponding β-spin transitions occur at 2472.1 and 2472.4 eV. Again, the splittings of 0.9 and 0.8 eV are underestimated compared to the experimental splitting of 1.3 eV but larger than the ground-state spin polarizations ($\Delta E_{\alpha-\beta} = 0.7$ eV).

Finally, the transitions to the empty ligand π* orbitals are predicted from 2473.6 to 2474.4 eV. Similar to complex **2**, the energies of these transitions are overestimated for $\mathbf{2^{ox}}$. Nevertheless, the trend of an increase in the transition energy upon oxidation from **2** to $\mathbf{2^{ox}}$ is faithfully reproduced by the calculation.

The most convincing result for the qualitative validity of an open-shell singlet ground-state description is the reproduction of the correct number of peaks by TD-DFT for the S K-pre-edge. For comparison, the theoretical S K-edge spectrum of the simple closed-shell singlet ground state from the nonbroken symmetry, spin-restricted calculation was computed. This ground state represents the delocalized $\{[Fe^{IV}\text{-dithiolene}^{2-}]^{2+} \leftrightarrow [Fe^{III}\text{-dithiolene}^{\bullet}]^{2+} \leftrightarrow [Fe^{II}\text{-dithiolene}^{0}]^{2+}\}$ description, indicating high covalency. In this electronic ground state, the antiferromagnetically coupled α- and β-spin electrons from the broken symmetry solution are not separated in space but occupy the same orbital, which is a linear combination of the d_{xz} and the ligand π_3* orbital. Consequently, no unpaired electrons are present in the molecule, and multiplet effects are not operative. The resulting spectrum is compared to the experimental and the broken symmetry spectra in Figure 17. In fact, only two peaks are observable in the pre-edge region in contrast to the experiment, which suggests that a closed-shell singlet is an inappropriate description for $\mathbf{2^{ox}}$.

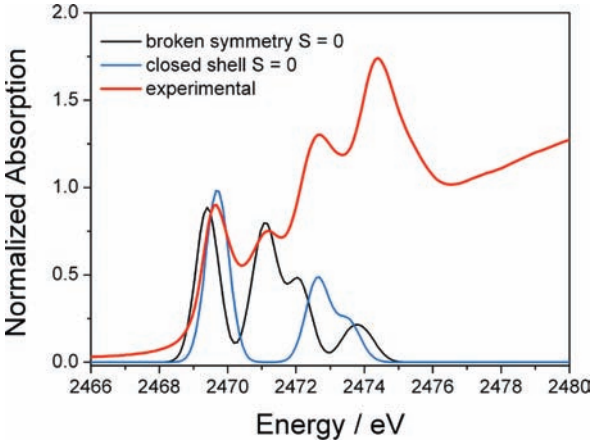

Figure 17. Comparison of the calculated BS(1,1) open-shell singlet and spin-restricted closed-shell spectra with the experimental data. A line broadening of 0.8 eV was assumed for the calculated spectra.

The calculated Fe K-pre-edge spectra of **2** and $\mathbf{2^{ox}}$ are shown in Figure S3 (Supporting Information) and important transitions are summarized in Table 6. Both spectra show a main feature at 7112.2 eV, which indicates that both iron centers possess the same oxidation state. The result is also consistent with the experimental spectra, which show only a very small shift of 0.3 eV upon oxidation. The additional shoulder at 7110.8 eV in the calculated spectrum for $\mathbf{2^{ox}}$ is not observed experimentally, which is most likely due to the large line broadening (core-hole lifetime) of the experimental spectrum.

The pre-edge feature of both complexes comprises five transitions to metal d orbitals: one transition to the t_{2g} set and four transitions to the two e_g orbitals, which are split by multiplet effects. The calculated splitting of the transitions to the d_{xy} and d_{z^2} orbitals in Fe K-pre-edge is very small (0.2−0.4 eV), which agrees with the experimental data; no resolved splitting of the pre-edge feature is observed for **2** or $\mathbf{2^{ox}}$. Note that for the calculated Fe K-pre-edge the magnitude of the multiplet splitting is smaller than the spin polarization of the ground state. This emphasizes that the calculated splittings are not exclusively a result of spin polarization but that additional effects in the excited state are important.

In summary, the TD-DFT calculations of the sulfur and iron K-pre-edge spectra reproduce the experimental spectra qualitatively and, thereby, confirm the electronic structures obtained from the DFT calculations. Even though the quantitative treatment of multiplet effects is not possible with the computational methods available for compounds of the size of **2** and $\mathbf{2^{ox}}$, the general trends are faithfully reproduced.

Conclusions

It is shown experimentally and DFT-computationally that the one-electron oxidized forms of the paramagnetic classical

Werner-type complexes $[Fe^{III}(cyclam)(tdt)]^+$ and $[Fe^{III}(cyclam)(mnt)]^+$ containing a low-spin ferric ion and a closed-shell neutral cyclam and a diamagnetic dianionic dithiolate(2−) ligand, namely, the dications $[Fe^{III}(cyclam)(tdt^{\bullet})]^{2+}$ and $[Fe^{III}(cyclam)(mnt^{\bullet})]^{2+}$, contain also a low-spin ferric ion and a closed-shell cyclam ligand and, in addition, an *S*,*S*′-coordinated, paramagnetic dithiolate(1−) π radical monoanion, $(tdt^{\bullet})^-$ and $(mnt^{\bullet})^-$, respectively. These dications, $\mathbf{2^{ox}}$ and $\mathbf{3^{ox}}$, are diamagnetic, and their electronic structure is best described as a singlet diradical which is composed of a low-spin ferric ion ($S_{Fe} = {}^1/_2$) coupled intramolecularly antiferromagnetically to a ligand π radical monoanion ($S_{rad} = {}^1/_2$) affording the observed $S = 0$ ground state. With the use of X-ray absorption spectroscopy supported by computational methods, this electronic structure is substantiated experimentally by the identification of multiplet splitting in the spectra of **2** and $\mathbf{2^{ox}}$. To our knowledge, this is the first time that such features have been observed in the pre-edge region of a sulfur K-edge spectrum. This is a rare example of direct experimental evidence for a singlet diradical as opposed to a closed-shell singlet in coordination compounds.

It is remarkable how similar the spectroscopic properties of $\mathbf{2^{ox}}$, $\mathbf{3^{ox}}$, and the corresponding *o*-benzosemiquinonate complex $[Fe^{III}(L\text{-}N_4Me_2)(dbsq)]^{2+}$ are. The latter has been structurally characterized.[46] The Mössbauer parameters (Table 4) and the electronic absorption spectra of these three complexes are also very similar. The same holds for the structurally characterized *o*-iminobenzosemiquinonate complexes $[Fe^{III}(cyclam)(L^{ISQ}{}_{1-3}{}^{\bullet})]^{2+}$ described in ref 30. We have found no evidence for the presence of Fe^{IV} in $\mathbf{2^{ox}}$ or $\mathbf{3^{ox}}$.

This and previous[1] work demonstrates that dithiolate(1−) π radical monoanions can be stabilized by coordination to first-row transition metal ions such as Cr^{III}, Fe^{III}, and Co^{III}.

Acknowledgment. We thank Prof. Frank Neese for helpful discussions about the DFT calculations and Dr. Stephen Sproules for assistance with XAS data collection. C.M. gratefully acknowledges the Max-Planck Society for a stipend. G.K.P. gratefully acknowledges the Department of Science and Technology, Government of India, for giving him a BOYSCAST fellowship (SR/BY/C-16/05). The Structural Molecular Biology program is supported by the National Institutes of Health (grant 5 P41 RR001209), National Center for Research Resources, Biomedical Technology Program, and by the Department of Energy, Office of Biological and Environmental Research.

Supporting Information Available: X-ray crystallographic files in CIF format of **1**, **2**, and **3**; Figure S1, showing the top view of the pairwise arrangement of the cations in the unit cell of $\mathbf{2}(PF_6)$; Figure S2, showing the comparison of the calculated S K-pre-edge spectra of **2** using different functionals; Figure S3, showing the calculated Fe K pre-edge spectra of **2** and $\mathbf{2^{ox}}$. This material is available free of charge via the Internet at http://pubs.acs.org.